Present Status and Future Opportunities of All-Perovskite Tandem Photovoltaics

Jin Wen[1]†, Hang Hu[2,3]†, Chao Chen[4]†, David P. McMeekin[5]†, Ke Xiao[1], Renxing Lin[1], Ye Liu[6], Henry J. Snaith[5]*, Jiang Tang[4]*, Ulrich W. Paetzold[2,3]* and Hairen Tan[1,6]*

[1]*National Laboratory of Solid State Microstructures, Frontiers Science Center for Critical Earth Material Cycling, College of Engineering and Applied Sciences, Nanjing University, Nanjing 210023, China*

[2]*Institute of Microstructure Technology (IMT), Karlsruhe Institute of Technology (KIT), Hermann-von-Helmholtz-Platz 1, 76344 Eggenstein-Leopoldshafen, Germany*

[3]*Light Technology Institute (LTI), Karlsruhe Institute of Technology (KIT), Engesserstrasse 13, 76131 Karlsruhe, Germany*

[4]*Wuhan National Laboratory for Optoelectronics (WNLO) and School of Optical and Electronic Information, Huazhong University of Science and Technology (HUST), Wuhan, Hubei, China.*

[5]*Clarendon Laboratory, Department of Physics, University of Oxford, Oxford, UK.*

[6]*Research and Development Center, Renshine Solar (Suzhou) Co., Ltd, Changshu, Suzhou, China.*

† These authors contributed equally to this work.

*Corresponding authors. E-mails: hairentan@nju.edu.cn; ulrich.paetzold@kit.edu; jtang@mail.hust.edu.cn; henry.snaith@physics.ox.ac.uk

All-perovskite tandem solar cells represent the forefront of next-generation photovoltaic technologies, offering a promising pathway to exceed the Shockley-Queisser efficiency limits of single-junction solar cells, while maintaining cost-effectiveness and scalability. However, transitioning from lab-scale prototypes to commercially viable products faces numerous challenges. Large-area fabrication requires developing scalable manufacturing techniques while minimizing performance losses compared to laboratory-scale spin-coating. Additionally, achieving long-term stability, reliability, efficient integration from cell to module, and high yield during practical deployment remain critical hurdles. This review addresses these key aspects, summarizes the latest field advancements, and highlights

strategies to overcome these challenges. By offering insights into the pathway toward reliable, durable, and high-performance all-perovskite tandem photovoltaics, this review aims to support their deployment in large-scale applications.

Introduction

The photovoltaic (PV) industry has witnessed remarkable progress in recent years, driven by significant cost reductions, efficiency improvements, and extended system lifetimes, making it one of the most competitive renewable energy sources. However, as silicon-based PV technologies mature, their record efficiency of 27.4% for crystalline silicon (c-Si) cells is nearing their practical theoretical limits of ~29.4%[1], leaving limited room for substantial efficiency gains within the c-Si PV technologies.

To overcome this limitation and further reduce the levelized cost of electricity (LCOE) for PV electricity generation, a multi-junction architecture approach exceeding the efficiency limit of single-junction devices is highly demanded[2]. A promising pathway towards this goal utilizes all-perovskite tandem solar cells, which leverage the ability of perovskite materials to flexibly tune their band gaps. This material property allows for two or more subcells with complementary bandgaps to be integrated into one solar cell device[3], as illustrated in **Box 1** (see a discussion of the figure details). This technology benefits from a reduction in photon thermalization losses, allowing for record certified power conversion efficiencies (PCEs) reaching beyond 30%, thus, outperforming single-junction silicon (27.4%) and perovskite (26.7%) solar cells[1]. Moreover, the certified mini-module efficiencies for all-perovskite tandems have reached 24.8%, surpassing the 23.2% efficiency of single-junction perovskite modules[1].

Beyond their exceptional efficiency, all-perovskite tandem solar cells benefit from abundant precursor materials, low-energy production and vapor or solution-processable fabrication, positioning them as a cost-effective alternative to Si-based PV. Moreover, the capabilities to manufacture tandem cells using low-temperature and scalable processing methods allow for diverse applications, ranging from lightweight and flexible panels to building-integrated photovoltaics. Combined with their potential for further efficiency gains, these unique properties position all-perovskite tandems as a pivotal technology for large-scale solar energy deployment. However, transitioning from laboratory prototype cells to commercially viable module products requires overcoming critical scalability, stability, and real-world reliability challenges.

This review provides a comprehensive overview of recent progress in all-perovskite tandem solar cells, focusing on strategies to improve the efficiency and address challenges in stability and scalability. It examines the mechanisms driving efficiency improvements, emphasizing the unique features and critical challenges of the p-i-n (positive-intrinsic-negative) architecture, also known as the "inverted" architecture of the wide-bandgap (WBG) and narrow-bandgap (NBG) subcells. It further explores material and structural factors influencing tandem stability, with a focus on emerging methodologies to improve durability. The next discussion extends to the transition from small-area devices to large-area modules, highlighting bottlenecks in large-area processing. Finally, the review suggests key directions for future research, offering a roadmap to advance all-perovskite tandem solar cells toward practical applications.

BOX 1| Typical architecture of all-perovskite tandem solar cells

All-perovskite tandem solar cells are classified into two main architectures: two-terminal (2T) and four-terminal (4T). The 4T design employs optical splitting or mechanical stacking, enabling each subcell to operate electrically independently. While this structure offers resilience towards spectral variations, it incurs a greater complexity and higher production costs, compared to 2T tandem solar cells, due to additional transparent electrodes and interconnection component. In contrast, the 2T architecture integrates both subcells into a monolithic stack with an interconnected tunnel recombination junction (TRJ), requiring a precise current matching for maximizing power output. This simple design facilitates integration into existing module frameworks and lowers production costs. However, its reliance on current matching can significantly limit the efficiency of the overall tandem if either subcell is considerably less efficient than intended. Additionally, stacking more than ten layers increases the complexity of the fabrication process, potentially reducing the production yield of the device. This results in the need for tight industrial and manufacturing processes.

The TRJ, typically composed of materials like metal oxides (*e.g.*, MoO_x, ITO) or ultrathin metal nanoclusters, enables efficient recombination between electrons (photo-generated from the top cell) and holes (photo-generated from the bottom cell). For realizing an efficient performance, the TRJ needs high vertical conductivity while minimizing lateral conductivity to prevent shunting. Ideally, the tandem device's open-circuit voltage (V_{OC}) equals of the V_{OC} of each subcell with minimal fill

factor (FF) loss[4]. Additionally, the TRJ requires high optical transmittance to minimize reflection and parasitic absorption losses, ensuring efficient light harvesting.

The tunability of the perovskite's bandgap allows for each of the subcells to achieve current match in a 2T tandem architecture. In ABX_3-type perovskites, the A-site is typically occupied by a mixture of cations such as cesium (Cs^+), formamidine (FA^+), and methylammonium (MA^+). Compared to adjustments at the A-site, the bandgap is controlled by the hybridization of the B-site cationic orbitals with the X-site anionic orbitals, and modifications at these sites can achieve the desired bandgap[5]. For 2T tandem solar cells, wide-bandgap (WBG, ~1.8 eV) perovskites are achieved by replacing iodide (I^-) with smaller halide ions such as bromide (Br^-) or chloride (Cl^-) at the X-site, while Sn doping at the B-site produces the narrow-bandgap (NBG, down to ~1.2 eV) perovskites, expanding the utilization of the near-infrared solar spectrum efficiently[6].

Research on 2T tandem architecture has gained considerable attraction, with rapid performance advancements[7–26]. The certified efficiencies for 2T tandems have now exceeded 30%[1], far surpassing those of single-junction perovskite solar cells (26.7%)[1,27–35] and 4T tandems (28.6%)[8,23,36–41]. Given the rapid progress and significant potential for commercialization, this review focuses on the advancements and challenges associated with 2T all-perovskite tandem solar cells and modules.

Strategies to exceed single junction efficiency limit

The recent efficiency advancements in all-perovskite tandem solar cells have been mainly driven by three key factors: innovations in TRJs (**Box 1 and Box 2**) and improvements in both WBG and NBG subcells (**Fig. 1a**). These breakthroughs were primarily rooted in an enhanced understanding of the p-i-n architecture of perovskite solar cells (PSCs), which has enabled significant efficiency gains in both subcells. Key factors contributing to these gains encompass: a significant reduction in non-radiative defects in the absorber layers, optimized surface passivation treatments, and improved charge-carrier transport layers to enhance the electron- or hole-extraction/transport properties, while suppressing surface recombination at that interface (**Fig. 1b and 1c**).

BOX 2| Performance evolution of all-perovskite tandem solar cells and modules

The figure illustrates the evolution of all-perovskite tandem solar cells and modules, focusing on key advancements in PCE and stability from 2016 to 2025. The development can be categorized into three distinct phases:

Early studies on all-perovskite tandem solar cells focused on finding suitable TRJ architectures and improving the crystallization of NBG subcells. Initial designs used the sputtered ITO as the TRJ and atomic layer deposition (ALD)-SnO_x as a buffer layer, achieving a PCE of 17.0%[8]. Subsequent advancements came to incorporating the evaporated MoO_x into Ag/ITO interfaces and Cl^- into NBG perovskites, increasing PCEs to over 21%[22]. Later, ALD-deposited SnO_2 layers paired with ultrathin Au nanoclusters created efficient TRJs, simplifying fabrication and enabling certified efficiencies of up to 24.8% in 2019[24]. This TRJ design has since become a mainstream choice for high-efficiency tandem architecture. However, at this stage, the operational stability (T_{90} represents the time required to degrade to 90% of the initial efficiency) of tandem devices remained below 500 h[24].

Efforts shifted to enhancing crystallinity and reducing defects in the perovskite absorber layer of each subcells to boost tandem performance since 2020. Key innovations included incorporating 4-trifluoromethyl-phenylammonium (CF_3-PA) into Pb-Sn perovskite precursors, extending carrier diffusion length, and achieving a certified tandem efficiency of 26.4% with T_{90} stability of 600 h[9]. Gentle gas-quenching methods controlled mixed-halide WBG crystallization, yielding a V_{OC} of 1.33 V, tandem efficiencies of 27.1%, and T_{80} stability of 1,825 h[11]. For tandem modules, the optimized WBG compositions enabled large-area fabrication with a module efficiency of 22.5% and a T_{80} stability of 500 h[42].

Research focused on interfaces between the perovskite and their respective hole or electron-transport layers (HTLs or ETLs) since 2022. These advances lead to a reduction in surface defects and improved energy level alignment, which contribute to improvements in both efficiency and stability. For WBG subcells, diammonium molecules were used to enhance surface states, achieving uniform surface potential and a tandem efficiency of 27.4%[10]. Depositing a lead-halide WBG perovskite layer on NBG subcells has created an advanced 3D/3D heterojunction that reduces non-radiative recombination and improves charge extraction, enabling tandem efficiencies exceeding 28% with T_{90} stability approaching 1,000 h[14]. Tandem modules also experienced

significant progress, achieving efficiencies up to ~25% through advanced crystallization of NBG perovskite and enhanced passivation at the buried interface, achieving T_{80} stability beyond 600 h[43].

Unique issues in NBG perovskites subcell

NBG perovskites present distinct challenges compared to Pb-based perovskites, including the intrinsic susceptibility of Sn^{2+} to oxidation, rapid crystallization leading to low-quality films, brittle contacts at the PEDOT:PSS/perovskite interface, and residual solvents within the perovskite films, especially at buried interfaces.

The oxidation of Sn^{2+} to Sn^{4+} is visually evident with a color change in the precursor solution and can also occur through more subtle mechanisms, such as solvent-mediated and charge-induced oxidation, resulting in an additional Sn vacancy (V_{Sn}) defects[44] (**Fig. 1d**). This process occurs even in trace oxygen and accelerates at 65–85°C due to the high reactivity and mobility of Sn^{2+}, making its retention intrinsically challenging. To address these issues, several redox-based strategies have been developed. Comproportionation, utilizing metallic Sn to reduce Sn^{4+} to Sn^{2+} in the precursor solution, extends the charge-carrier diffusion length in Pb-Sn perovskites and achieves PCEs exceeding 21%[24] (**Fig. 1e**). Amphiphilic antioxidants with surface-anchoring properties, such as formamidinium sulfonic acid (FSA), enhanced film uniformity, yielding a PCE of 21.7%[25]. Additionally, electron-withdrawing ligands like chloromethyl phosphonic acid (CMP) mitigated Sn oxidation[15], reducing defect density and achieving efficiencies of 21.65% with a V_{OC} of 0.852 V. Recently, multifunctional additives such as 2-amino-3-mercaptopropanoic acid hydrochloride (AMPH) and Thiomalic acid (TA)[45,46], which contain functional groups like the thiol group (-SH), a carboxylic acid group (-COOH), and an ammonium group ($-NH_3^+$), have been designed to prevent Sn^{4+} formation and pushed the PCE of NBG subcells to around 23%.

Driven by the high Lewis acidity of Sn^{2+} and its fast coordination with organic components, the rapid crystallization of NBG perovskites pose significant challenges in fabricating high-quality films. This process often produces small grains with high-density grain boundaries that might act as nonradiative recombination centers and trap sites (**Fig. 1f**). Additionally, Sn alloying induces grain contraction, leading to residual strain that exacerbates defect formation and hinders charge extraction[47]. The weak Sn-I bonding compared to Pb-I further causes organic cation depletion at the film surface, increasing the trap density. Key innovations have focused on optimizing charge transport and defect passivation to address these issues. Incorporating CF_3-PA into the precursor

solution significantly extended the carrier diffusion length to over 5 μm, enabling the fabrication of thicker NBG perovskite layers (up to 1.2 μm)[9]. This advancement improved the short-circuit current density (J_{SC}) and efficiencies exceeding 22% for NBG subcell, contributing to a certified tandem efficiency of 26.4% that surpassed those of single-junction perovskite solar cells for the first time. It is noteworthy that to ensure adequate light absorption, the thickness of the NBG perovskite layer typically needs to exceed 1 μm. However, due to incomplete solvent quenching, this can result in residual solvents at buried interfaces, which may compromise device stability.

Another noteworthy approach involves introducing quasi-two-dimensional (quasi-2D) structures, such as $(PEA)_2GAPb_2I_7$, by using mixed bulky organic cations like phenethylammonium (PEA^+) and guanidinium (Gua^+)[48]. These structures effectively passivated defects and enhanced the structural and optoelectronic properties of 1.25-eV Pb-Sn perovskites. These advancements addressed crystallization-induced defects and charge transport limitations, enabling NBG subcell efficiencies exceeding 22% and tandem cell efficiencies up to 25.5%.

Unique issues in WBG perovskites

For WBG perovskite subcells, the experimentally reported V_{OC} have consistently fallen short of theoretical maximums compared to normal-bandgap devices[49]. Recent advancements in understanding the underlying causes of V_{OC} losses have shifted the focus beyond just phase segregation due to high Br content. While phase segregation remains a critical issue for long-term stability (discussed in the next part), the increased V_{OC} in WBG perovskite films is often linked to deep trap states induced by halide interstitials[50]. A higher Br content can amplify the formation of transient hole traps, adversely impacting quasi-fermi level splitting (QFLS) and thus photoluminescence quantum yields (PLQY)[51] (**Fig. 1c**). Density functional theory studies have shown that halide interstitials are thermodynamically stable and contribute significantly to the formation of deep trap states[52]. Advanced characterization techniques such as photoemission electron microscopy and multimodal operando microscopy have been developed to enable nanoscale mapping and spatial correlation of charge transport losses, recombination losses, and chemical composition, providing critical insights into the spatial heterogeneity within perovskite films and the origins of performance limitations[53,54]. Non-radiative recombination pathways are particularly pronounced at grain boundaries and surfaces in perovskite films, which is driven by the complex crystallization kinetics of mixed cations and halides.

Addressing the above challenges requires strategies to either homogenize the crystallization process or effectively passivate surface and bulk defects. Notably, gas quenching has been highly effective for producing components with higher Cs^+ content, resulting in an improved structural quality and higher V_{OC}[11,55,56](**Fig. 1g**). A promising approach involves a film-side-down close-space annealing (CSA) process, in which solvent release was precisely controlled, resulting in high-quality perovskite absorbers with micrometer-scale grains and prolonged carrier lifetimes[36]. For WBG perovskites, additive strategies such as incorporating 2D passivation, chloride or pseudohalide-based salts, and multifunctional small molecules[57] have been employed to regulate film morphology and reduce defect states. Despite these advancements, the inherent crystalline heterogeneity of WBG materials still results in more significant losses compared to the highly crystalline quality of $FAPbI_3$ films, underscoring the need for further exploration and refinement.

Interface engineering in p-i-n structure

Following reducing bulk defects, strategies have increasingly focused on reducing non-radiative recombination between the perovskite and HTL or ETL interfaces. High-density traps at perovskite heterojunction interfaces, often formed by unpassivated dangling bonds, are among the primary causes of recombination losses[58]. By tailoring the terminal groups at the perovskite interface, surface modification effectively reduces defects and further improves charge extraction.

Perovskite-ETL interface

Various surface modification techniques have substantially improved the performance of p-i-n PSCs by addressing two critical aspects: (1) forming heterojunctions to induce n-type properties in the top surface region, facilitating efficient charge transfer (**Fig. 1h**), and (2) reducing surface defects to minimize recombination losses (**Fig. 1j**). For instance, strategies to create a type-II band alignment at the Pb-Sn perovskite/ETL interface have been employed to suppress the undesired p-type doping concentration, reduce defect-induced surface recombination velocity (SRV), and improve electron extraction[14] (**Fig. 1i**). These approaches have enabled Pb-Sn perovskite solar cells with 1.2-μm-thick absorbers and thus achieving high PCE of 23.8%, with a V_{OC} of 0.873 V and a FF of 82.6%[14]. Further research has revealed that mixed Pb-Sn perovskite films often exhibit compositional gradients with excess Sn at the top surface, leading to oxidation and accelerated recombination rates[16]. Diamines have been used to chelate Sn atoms to address this issue,

achieving a more balanced Sn stoichiometry. This strategy forms a low-resistance barrier layer that passivates defects, enabling efficiencies of up to 23.9% in NBG devices.

Optimizing the perovskite/ETL interface has also improved V_{OC} and FF in WBG subcells for tandem architecture. Three main strategies have been developed: (1) anchoring functional materials on the perovskite surface and constructing (2) low-dimensional or (3) heterostructured materials atop the perovskite absorber. Organic salts like guanidinium bromide (GuaBr), phenethylammonium iodide (PEAI), butylammonium bromide (BABr), and 4-(trifluoromethyl)phenylethylammonium are widely used as passivation to stabilize the perovskite surface and reduce non-radiative recombination losses[59–61]. An effective surface reconstruction strategy was developed to fabricate a high-quality NBG perovskite surface with a close-to-ideal stoichiometric ratio via using 1,4-butanediamine (BDA, for minimizing Sn^{4+} related defects) and ethylenediammonium diiodide ($EDAI_2$, for passivating organic cation and halide vacancy defects)[17]. Co-modifiers like diammonium combined with methylthio or phenylethylammonium molecules have also demonstrated selective passivation for defect states, reducing trap-assisted recombination in both WBG and NBG perovskites[62,63] (**Fig. 1k**). Furthermore, diammonium has been reported to enhance the orientation of [6,6]-phenyl-C_{61}-butyric acid methyl ester (PCBM), thereby minimizing nonradiative recombination at the perovskite/ETL interface[64]. A recent strategy using a mixture of MAI and PEAI in the anti-solvent enabled the fabrication of WBG perovskites with enhanced (100) plane orientation, achieving a certified tandem PCE over 29%[18]. This method promotes 2D (n = 1) layered perovskite formation, oriented nucleation, and downward crystal growth, reducing non-radiative recombination in the bulk and interfaces. In addition to organic interface engineering, ultrathin dipole layers, such as MgF_2 or LiF, inserted at the perovskite/C_{60} interface mitigated non-radiative recombination and enhanced device performance[65].

Perovskite-HTL interface

The buried perovskite/HTL interface poses a significant challenge for p-i-n PSCs. High density of deep trap states at this interface have been revealed through mechanical and chemical delamination methods[66,67](**Fig. 1l**). Advances in HTLs, such as replacing traditional PEDOT:PSS with multifunctional materials like MPA2FPh-BT-BA (2F, **Fig. 1m**), have led to improved energy level alignment, regulated perovskite growth, and effective defect passivation[13]. Specifically, 2F utilizes

a benzoic acid anchoring group to replace the traditional 2-cyanoacrylic acid, improving molecular stacking and face-on orientation on ITO surfaces, while the introduction of fluorine atoms deepens the highest occupied molecular orbital (HOMO) level. Another designed SAM with oligoether side chains was custom-introduced on the benzothiadiazole unit by the same research group, pushing the efficiency of NBG subcells to 23.54%[68]. Since 2022, self-assembled monolayers (SAMs) anchored on transparent conductive oxide (TCO) or nickel oxide (NiO_x) as HTLs have emerged as a mainstream HTLs in WBG subcells[69], replacing traditional conductive polymers like (poly[bis(4-phenyl) (2,4,6-trimethyl-phenyl)amine) (PTAA) and N4,N4′-di(naphthalen-1-yl)-N4,N4′-bis(4-vinylphenyl)biphenyl-4,4′-diamine (VNPB). Early studies on SAMs, such as (2-(9H-carbazol-9-yl)ethyl)phosphonic acid (2PACZ) and Me-[4-(9H-carbazol-9-yl)butyl]phosphonic acid (Me-4PACz) demonstrated enhanced hole extraction and reduced interface traps, significantly reducing voltage losses in WBG devices. Subsequent development of SAMs, including (4-(7H-dibenzo[c,g]carbazol-7-yl)butyl)phosphonic acid (4PADCB), has further optimized the passivation efficacy, energy level alignment, and surface wettability, resulting in superior device performance[70].

Despite these advancements, the passivation of the buried interface has received less attention than the perovskite/ETL interface, mainly due to the solubility of passivation materials in perovskite precursor solvents. A doping strategy using chiral aspartate hydrochloride (AspCl) at the PEDOT interface was developed to address this limitation. This approach forms intermolecular hydrogen bonds throughout the perovskite film, enabling an efficiency of 22.46% in Pb-Sn perovskite solar cells[12]. Beyond doping HTLs with pre-embedded passivation molecules, glycine hydrochloride (GlyHCl) additive was utilized to passivate the buried perovskite/ETL interface and improve the quality of the underlying perovskite layer, as the large-size $GlyH^+$ cations preferentially settle to the bottom during crystallization[70–72]. From another perspective, a vapor-solution two-step method appears more suitable for bottom-surface passivation. However, this approach currently yields lower-quality perovskite films than the one-step spin-coating method, highlighting a need for further optimization.

Operational stability of all-perovskite tandem solar cells

As the efficiency of all-perovskite tandem solar cells surpasses the 30% benchmark, device stability becomes a critical issue, which is currently hindering their commercial potential. In recent

years, significant progress has been made in enhancing the operational lifetimes of all-perovskite tandem solar cells (**Fig. 2**) through material design, crystallization regulation, defect passivation, and device structure optimization. Among these advancements, the most notable breakthroughs include mitigating halide segregation in WBG perovskites, optimizing the composition and structure of NBG perovskites, and developing robust interconnection layers. This section highlights these key developments and their role in advancing device stability.

Light-induced halide segregation in WBG perovskites

WBG perovskites are more susceptible to halide segregation under continuous illumination, driven by photoinduced polarons and halogen ion migration[73,74]. This segregation forms I-rich and Br-rich regions, where photocarriers become trapped in low-bandgap I-rich domains, increasing non-radiative recombination loss. The phenomenon is further exacerbated by lattice defects, grain boundaries, and residual stress (**Fig. 2a**), underscoring the need for thermodynamically stable compositions and high-quality films.

Bulk strategies to address halide segregation focus on two main approaches: adjusting compositions to increase the activation energy for halide migration and reducing defects to suppress ion migration pathways (**Fig. 2b**). Recent studies have highlighted that halide segregation is not solely determined by Br content–the A-site cation also plays a significant role in the overall lattice structure[75,76]. While incorporating Cs enhances stability, it will introduce deep-level defects due to its size mismatch with FA^+. To mitigate this, larger A site cations (e.g., DMA^+, Gua^+, and EA^+) have been introduced to reduce lattice strain and defect densities[77,78]. At the X-site, Cl^- doping has been shown to increase the halide migration barrier by alleviating lattice microstrain, thereby stabilizing the lattice framework[79]. A representative composition, $Cs_{0.4}FA_{0.5}DMA_{0.1}Pb(I_{0.72}Br_{0.23}Cl_{0.05})_3$, achieves a bandgap of 1.8 eV with an optimized PCE and improved photostability, with T_{90} over to 1,000 h[55] (**Fig. 2c**).

Defects in WBG perovskite films act as low-energy pathways for ion migration, significantly reducing operational lifetimes. Theoretical studies indicate that phase segregation often originates at grain boundaries, where defect vacancies are concentrated[80]. Crystallization regulation strategies to address these issues have been covered in the previous section. Here, we highlight the critical role of interfaces in governing the photostability of WBG perovskite devices. Interfacial defects not only increase non-radiative recombination, thereby reducing efficiency but also lead to

carrier accumulation within the perovskite layer, often resulting in irreversible degradation[81,82]. Studies have shown that under short-circuit conditions, where carrier accumulation is minimized, phase segregation in WBG perovskites is significantly suppressed[83]. In contrast, under open-circuit conditions, carrier accumulation can induce the formation of polarons, which amplify phase segregation and accelerate degradation[84]. This phenomenon explains the disparity between experimental observations of phase segregation occurring within minutes in thin films and the T_{90} operational lifetimes of WBG devices, which can extend to several hundred hours under real-world conditions.

As the dominant HTLs in WBG subcells, SAMs can be further optimized by mixing multiple types to improve energy level alignment, enhance carrier collection, and ultimately boost the stability of WBG perovskite devices. However, their single-molecule anchoring mechanism can result in localized microscopic non-uniformity and susceptibility to solvent-induced detachmen[85,86]. Moreover, their long-term thermal stability remains uncertain, with potential risks of substrate delamination or desorption under prolonged stress. It is also worth exploring that the intrinsic stability of transport layers cannot be equated to their stability when integrated into devices. For example, while NiO_x exhibits excellent intrinsic stability, their interfaces with perovskites often suffer from chemical reactions and significant defects, making them a primary source of degradation[87]. Striking a balance between these factors remains a key challenge for future research[88-98].

Incorporating thin, low-dimensional perovskite layers into top interfaces has enhanced stability, leveraging the hydrophobic nature of large organic cations and their higher ion migration barriers. However, conventional spin-coating methods often yield a 2D layer with n =1 due to a solvent-driven surface-reconstruction displacement reaction. While n =1 layers at the upper interface facilitate hole transport in n-i-p configurations, their energy level alignment impedes electron transport at the C_{60} interface in p-i-n architectures, diminishing the stability gains of the 2D layer. To address this, several strategies have been developed to form higher-n 2D layers with more appropriate energy level alignment: such as solvent modulation during passivation, avoiding thermal annealing, and in situ formation via evaporated PbI_2 on the surface[99–101]. These approaches improved energy level alignment and enhanced electron transport while optimizing stability and device performance, enabling the T_{90} of WBG subcell to reach up to 1,700 h[84].

Stability issues in NBG perovskites

The oxidation of Sn^{2+} and the rapid crystallization leading to high defect states (**Fig. 2d**), discussed in the efficiency section, are also strongly linked to stability and are not reiterated extensively here[102-104]. Although methylammonium (MA^+) ions have been shown to enhance stability in specific scenarios, their inclusion at levels exceeding 30% in high-efficiency NBG compositions poses considerable stability risks[105-111]. The volatility, hygroscopicity, and thermal instability of MA^+ significantly compromise device durability, particularly under elevated temperatures such as the 85°C conditions specified in IEC standards. To address these issues, pure FA-based Pb-Sn perovskites were developed, achieving efficiencies of 21.0% in single-junction cells and 26.3% in all-perovskite tandem, with T_{90} of 212 h thermal stability at 85°C under dark[107]. Incorporating Cs into FA-based systems further enhanced thermal robustness, giving rise to double- and triple-cation compositions such as FACs and FARbCs[112]. These systems demonstrated improved resistance to light and humidity, with stabilized efficiencies and significant gains in long-term operational stability. For instance, advanced RbCsFA compositions have achieved a record efficiency of 24.13% and thermal stability T_{90} of 795 h[113]. All-inorganic $CsPb_{0.4}Sn_{0.6}I_3$ perovskites have also shown promise, offering superior thermal stability, with T_{80} exceeding 1,510 h at 65°C and 800 at 85°C, despite relatively lower efficiencies of 17.4%[114]. These results highlight the potential for further optimization of inorganic compositions.

The acidity of PEDOT:PSS, a commonly used HTL, negatively impacts device stability by damaging the brittle interface and creating detrimental recombination centers. Modifications to PEDOT:PSS, such as p-guanidinobenzonitrile hydrochloride treatment, have improved performance, achieving a PCE of 23.3% with a T_{80} of 300 h[115]. Exploring alternatives to PEDOT:PSS is a valuable direction. Additives like multifunctional ammonium sulfide (MAS)[116], oxalic acid (OA)[117], and acetylcholine chloride (ACh) have been used to modify PEDOT:PSS[40], achieving PCE over 24% in NBG subcell. These strategies have also demonstrated efficiencies of ~28% with a T_{80} of 500 h under MPP conditions for all-perovskite tandem. SAMs are another promising approach for Pb-Sn devices, yielding a PCE of 23.46% with a T_{88} of 590 hours at 65°C[70]. Impressively, GeI_2-modified NiO_x achieved a PCE of 23.34% with storage stability exceeding 4,320 h in N_2[111]. A novel HTL, P3CT, with a higher pK_a, overcame interface degradation and

enabled tandem to retain 96% of their initial PCE after >1,000 h of MPP testing under ambient conditions (**Fig. 2d and 2f)**, representing the best stability performance to date for this device type[118].

Stability issues from interconnection layer

While the SnO_2/ultra-thin Au/PEDOT:PSS configuration is the mainstream TRJ structure for all-perovskite tandem, concerns about the scalability of this design arise due to the potential interfacial diffusion of Au clusters during prolonged operation (**Fig. 2g** and **2h**). To address these concerns, various interconnection layer innovations have been proposed to enhance stability[119-121]. One promising alternative is the SnO_2/NC-ITO/SAMs structure, which combines high transparency and excellent electrical conductivity. The NC-ITO layer was fabricated using a low-temperature solution-processing method, reducing damage to the underlying subcells and demonstrating superior stability with T_{95} of 550 h[121] (**Fig. 2i)**. Another widely used TRJ configuration is the SnO_2/sputtered-TCO/PEDOT structure, where sputtered TCO films such as ITO and IZO provide high transparency and conductivity[70,120]. In perovskite-organic tandem cells, a sputtered IZO layer sandwiched between BCP or SnO_x and MoO_x has achieved record PCEs of 24% by minimizing optical and electrical losses[122,123]. However, the sputtering process, particularly at high temperatures or with high-energy particles, risks irreversible damage to the underlying perovskite subcell and limits its adoption in high-efficiency all-perovskite tandem devices.

A novel approach employs an n-SnO_2/p-SnO_{2-x} TRJ, leveraging the bipolar properties of SnO_x for efficient electron and hole transport[118]. The simplified C_{60}/SnO_{2-x} interconnection layer further improves the efficiency and photostability of 2T all-perovskite tandems by reducing reliance on complex TRJ structures and minimizing sputtering-induced damage. However, the need for precise control of pulse and reaction times to achieve the optimal Sn:O ratio has hindered its widespread application.

Perspective for stability research

Current stability research for tandem devices lags behind that for single-junction cells, with most studies limited to International Summit on Organic Photovoltaic Stability (ISOS) protocols[124]. Although both NBG and WBG subcells generally adhere to established standards, the absence of specialized stability protocols for all-perovskite tandem solar cells presents a critical issue. Current ISOS protocols, designed for conventional single-junction devices, use single-stress tests (like

light, heat, or moisture alone), failing to mimic the multistress conditions (such as simultaneous light, heat, and electrical bias) found in real-world environments. Moreover, achieving tandem efficiency crucially depends on precise current matching, yet there is inconsistency in the light sources used in studies (e.g., a two-lamp high spectral match solar simulator vs. a white LED), leading to skewed results in interlaboratory stability and performance comparisons.

Module-scale tandems face their own set of challenges, such as interlayer delamination due to thermomechanical stresses, halogen outdiffusion across subcell interfaces, and encapsulation failures under combined humidity-thermal cycling. The current ISOS protocols, such as ISOS-T for thermal aging, do not sufficiently cover tandem-specific degradation modes, including voltage-mismatch-induced leakage currents or subcell-selective degradation under partial shading. Several urgent standardization efforts are necessary: (1) Material/subcell-level tests (e.g., UV-resistance for WBG, reverse-bias endurance for NBG); (2) Tandem-level protocols that enforce spectral consistency, validate dynamic current-matching, and simulate multiple stresses; (3) Module-level standards at outdoor condition that ensure the robustness of encapsulation and the durability of interconnects. Proposing a specialized ISOS-Tandem subclass within the ISOS framework, in collaboration with industry partners, could standardize testing procedures and expedite the commercialization of perovskite tandem cells.

While efficiency improvements in perovskite devices have progressed rapidly, stability analysis remains more complex and time-intensive. Strategies such as introducing additives or interface treatments often enhance efficiency but do not always improve stability, highlighting the need for tailored approaches. Advanced in-situ tools like photoelectron microscopy and synchrotron radiation will be critical for providing dynamic, high-resolution insights into perovskite behavior under operational conditions. Looking ahead, high-throughput research methods integrated with machine learning could redefine stability studies. By enabling large-scale data collection and analysis, these approaches may help identify molecular candidates that simultaneously enhance stability and efficiency, accelerating material and device optimization.

Challenges and Innovations in Upscaling Production

Most all-perovskite tandem PSCs reported with high PCEs are based on lab-scale small area (<1 cm^2) in 2T architecture (see details in **Box 2**), which stimulated scaling up to over 1-cm^2 area and even mini-module dimension of >10 cm^2 (**Fig. 3a**). In this section, we focus on the upscaling of

2T all-perovskite tandem devices. Improving PCEs of large-area all-perovskite tandem devices by scalable methods is challenging, since upscaling from small area to large size induces new complexities, such as sequential scalable processing, film homogeneity, interfacial quality, charge transport/collection, and module designs.

Upscaling of over 1 cm^2 tandem solar cells

The early stage of upscaling all-perovskite tandem achieved a PCE of approximately 24% by employing a novel hole transport layer, NiO_x/VNPB, and using FSA to regulate the crystallization of NBG perovskites[25]. In 2023, ~1 cm^2 tandem solar cells benefited from a significant research momentum of SAM HTL in WBG perovskite subcell[70] (**Fig. 3b**), pushing PCEs up to >26% with enhanced V_{OC} of >2.1 eV. Compared to ~0.1 cm^2 small-area devices, ~1 cm^2 tandem solar cells suffer severe PCE loss due to surficial inhomogeneity, especially at the perovskite/ETL interface. Recently, several novel strategies achieved uniform passivation, such as forming 3D/3D or 2D/3D bilayer perovskite heterojunction (using thermal evaporation), Dion-Jacobson or Ruddlesden-Popper 2D phases, realizing a groundbreaking certified PCE up to 28.2% on ~1 cm^2 area[125]. These breakthroughs narrowed the absolute PCE gap to <1.5% for upscaling from ~0.1 to ~1 cm^2 levels, providing promising pathways to large-sized module fabrication.

Scalable processing of tandem solar modules

Scaling up perovskite films to large-area module dimensions necessitates moving beyond spin coating to scalable and cost-effective methods such as slot-die coating, blade coating, thermal evaporation, spray coating, and inkjet printing. The currently reported high-efficiency devices are all prepared using the blade-coating method (**Fig. 3b**). Functional layers, including charge transport layers and TRJs, can be deposited using techniques like thermal evaporation, blade coating, ALD, and sputtering.

The development of all-perovskite tandem solar modules has lagged behind single-junction solar modules and small-area (<1 cm²) tandem solar cells (**Fig. 3b**). Only a few prototypes have been demonstrated to date[42,43,126–128], reflecting the significant challenges in transitioning to fully scalable processing for large-area substrates. Sequential deposition of multiple layers (>10) and the control of perovskite crystallization for both WBG and NBG layers are critical hurdles. Additionally, transitioning from spin-coating to scalable techniques and scaling up from ~1 cm² to module-sized areas present significant barriers to achieving high performance (**Fig. 3b**).

Despite these challenges, advancements in module design and scalable coating technologies have enabled an all-perovskite tandem solar mini-module to achieve a certified aperture-area PCE of 24.5%, surpassing the current record of 23.2% for single-junction solar mini-modules. The following sections will explore the key factors driving this performance improvement.

Key parameters of efficiency losses for modules

The module $V_{OC,module}$ is the sum of the V_{OC} of all sub-cells. $V_{OC,module}$ loss mainly originates from the scalable coating quality of the large-area perovskite layer that is dominated by morphological homogeneity, crystal quality, thickness uniformity, and interfacial quality. The module short-circuit current ($I_{SC,module}$) is determined by the smallest I_{SC} of sub-cell. $I_{SC,module}$ loss is mainly associated with geometric fill factor (GFF, i.e., the proportion of active area to aperture area, **Fig. 3c**) and internal series resistance (R_S) of the entire module.

P1 and P3 scribes isolate, while P2 scribes connect adjacent sub-cell electrodes. Accurate control of P2 scribe width is crucial; excessively wide scribes decrease the GFF, and overly narrow ones increase resistive losses due to incomplete layer removal, TCO damage, debris redistribution, or metal-halide interactions[129] (**Fig. 3c**). A thin conformal diffusion barrier layer, i.e., ~10 nm ALD-SnO_x, was employed after P2 scribing process to prevent the interfusion between Ag electrode and I^-, simultaneously forming good ohmic contact with low vertical resistance at the ITO/ALD-SnO_2/Ag junction and also improving the device stability[42]. This also isolated Ag and PEDOT:PSS in the recombination junction, enhancing shunt resistance. Optimized laser scribing (e.g., pulse energy, frequency, and speed) ensures uniform ablation, complete layer removal, and avoids TCO damage. Additionally, air-exposure degradation, particularly in NBG perovskites, must be addressed during module fabrication.

Control of perovskite crystallization in scalable processing

Perovskite film quality and homogeneity are controlled by crystallization kinetics that involves a classical theory of nucleation and crystal growth[130-138] (**Fig. 3d**). In general, two pathways involve in the first step: homogeneous (*i.e.*, the nuclei generated within the precursor without any preferential sites) and heterogeneous nucleation (*i.e.*, the nuclei preferentially form in specific regions, such as on the substrate surface, at defect sites, or around impurities)[139].

One of the critical challenges is the inherent uncontrollable rapid crystallization of Sn-based perovskites that induces complexity and difficulty in the blade-coating process[140]. The higher Lewis acidity of Sn^{2+} and lower solubility of SnI_2 (in DMF/DMSO solvent system) make the crystallization conditions more stringent and induce a narrow processing window, *e.g.*, Sn-based perovskites are capable of crystallizing at room temperature, unlike Pb-based perovskites requiring post-annealing. In addition, the difference in dynamic crystallization kinetics and thermodynamic stability creates competition between Sn and Pb, resulting in an inhomogeneous distribution throughout the perovskite film (e.g., imbalanced stoichiometry of Sn and Pb). Therefore, the uncontrollable properties of rapid crystallization generally led to poor homogeneity, increased defect density, and low crystalline quality. These also explain scalable processing of NBG perovskite films is currently a key production bottleneck for the advancement of all-perovskite solar modules (**Fig. 3e**). A moderate nitrogen flow (260 cm^3 min^{-1}) was employed for fabricating 12.25 cm^2 NBG perovskite film, resulting in an accelerated mass transport from the NBG perovskite surface and improved crystallization. It produced a uniform morphology free of defects and pinholes (**Fig. 3f**), achieving a PCE of 19.1% in scalable mini-modules[128]. To blade coat a thick (~1 μm) NBG perovskite film, the as-fabricated wet film also required to be thick. However, the trapped DMSO (high boiling-point solvent) near the buried interface induces the interfacial voids due to the top-to-bottom crystallization direction[43,126]. To avoid the void formation, the reduced molar ratio of DMSO (optimum of 8%, referred to Pb and Sn) was utilized in the precursor, resulting in enlarged grain sizes and void-free buried interface[126] (**Fig. 3f**). This enabled efficient all-perovskite tandem solar modules delivering a PCE of 21.6% over a 14.3 cm^2 aperture area. It is also found that the wettability of NBG perovskite becomes worse on top of large-area PEDOT:PSS substrate with the decay of coating time, leading to non-uniform nuclei density subsequent to uneven solvent extraction. Therefore, it is crucial to extend the processing window of blade coating as it is a time-demanding step. A novel additive AAH was employed to retard the crystallization as it coordinates strongly with precursor. The processing window was extended up to 100 s without performance loss due to high homogeneity and quality of NBG perovskite films[43] (**Fig. 3f**). AAH was also demonstrated accumulation at the buried interface with passivating defects. Fully scalable all-perovskite tandem solar modules achieved a certified PCE of 24.5% with 20.25 cm^2 aperture area (**Fig. 3b**). This approach also reached a high PCE of 23.8% with 64

cm^2 aperture area (**Fig. 3e**). Recently, the same group released a record certified PCE of 24.8% over 64 cm^2 aperture area[1].

Scalable processing of WBG perovskite films remains challenging. Mixed-halide WBG perovskites exhibit diverse crystallization kinetics, often accompanied by phase heterogeneity issues[42,97]. Additionally, Cs and Br salts have limited solubility in polar aprotic solvents, such as DMF and DMSO. These constrain the scalable processing of large-area WBG perovskite films for module production. In response, the nucleation was controlled by varying the Cs content. The optimized composition of $Cs_{0.35}FA_{0.65}PbI_{1.8}Br_{1.2}$ realized enlarged grain sizes, improved film homogeneity, and reduced phase segregation[42]. A certified PCE of 21.7% was achieved in mini-modules (**Fig. 3e**). Some additives (such as methylammonium thiocyanate[134] and glycine amide hydrochloride[96]) were also employed for regulating crystallization in the blade-coating process. Very recently, green-solvent scalable fabrication was developed in all-perovskite tandem solar modules. For replacing DMF, a green solvent system composed of DMSO/acetonitrile (ACN)/ethyl alcohol (EtOH) was developed to extend the processing window and avoid void formation at the buried interface[127] (**Fig. 3f**). With utilizing green solvents in WBG perovskite precursor, a high PCE of 23.8% was reached in the tandem modules. The green solvent system was also demonstrated upscaling capability in NBG perovskite fabrication. As a result, the mini-module based on fully green solvents for processing of both WBG and NBG perovskites realized a PCE of 22.2% (**Fig. 3e**). The PCE gap (**Fig. 3b**) was attributed to the Sn^{2+} oxidation caused by DMSO as a higher ratio of DMSO was used in green solvent system[92]. The achievement opens the door for environmentally friendly production of all-perovskite tandem modules.

Perspectives and outlooks

As highlighted in the previous section, all-perovskite tandem solar cells have garnered significant research interest in recent years. This section will discuss potential directions for future exploration, key challenges, and outlooks.

Multijunction configurations for enhanced efficiency

Multi-junction architectures represent transformative strategies for surpassing the efficiency limits of tandem devices by harnessing a broader portion of the solar spectrum[141-142]. The theoretical efficiency limit increases toward more junctions in combination with optimum bandgaps (**Fig. 4a**). Unlike the high-cost III-V multi-junction cells, perovskite-based multi-junction solar cells offer a

cost-effective and high-performance alternative for terrestrial applications. However, additional subcells introduce new complexity and challenges such as sequential processing, device architectures, the interaction between the multi-layer stacks, the choice of ultra NBG perovskites, stability, and upscaling. It is noteworthy that the lowest perovskite bandgap (down to ~1.2 eV) impedes the development of all-perovskite multi-junction PVs, e.g., at least two subcells need the optimum ultra-narrow bandgaps <1.15 eV for four or even more junctions. Very recently, a new benchmark for multi-junction PV was achieved by enhancing Pb-Sn perovskite films with amino acid salts, which synergistically improved film quality and optoelectronic properties, leading to record PCEs of 28.7% for triple-junction and 27.9% for quadruple-junction devices[143]. Despite these advances, significant gaps remains in reaching the practical efficiency potential of 37%[142] (for ideal bandgaps of 1.2/1.5/2.0 eV).

These differences between theoretical and experimental efficiencies are primarily attributed to the performance limitations in WBG (2.0 eV) top cells, where high Br content complicates film quality. Due to the versatility of WBG cells, the optimization of all-perovskite multi-junction devices often aligns with advancements in perovskite/Si and perovskite/organic multi-junction technologies. Emerging strategies to overcome these challenges include the use of halogenated diammonium salts and propane-1,3-diiodide as additives to enhance halide homogeneity. Compositional engineering—such as replacing Cs^+ with Rb^+ at the A-site and introducing halogenocyanate (OCN^-) at the X-site—has shown promise in alleviating lattice strain[144-145]. Realizing the full potential of multi-junction will require continued optimization of subcell performance, complemented by advanced light management techniques, including anti-reflective coatings and photonic structures, to ensure optimal photon utilization and current matching.

Real-world optimization with structure design

The real-world performance of all-perovskite tandem PVs depends on adapting to variables such as tilt angles, tracking methods, and climatic factors, including solar spectra and humidity[146]. Considering albedo irradiation in realistic irradiation conditions, the bifacial tandem PV retains a higher energy yield gain compared to the monofacial PV[147]. For bifacial tandem modules, effective light management becomes critical to achieve current matching and maximize energy capture from both direct and diffuse light (**Fig. 4b**). Advanced strategies such as bandgap tuning[148] (**Fig. 4c**),

angular response optimization, and thermal management systems are being developed to address these challenges.

A key hurdle under field test conditions (FTCs) is "current mismatch", where varying angles of incidence (AOI) and spectral shifts disrupt subcell photocurrent balance. Unlike the controlled conditions of standard test protocols, FTCs expose devices to dynamic thermal effects, wind, and humidity, which can alter perovskite bandgaps and exacerbate mismatch. Despite these challenges, tandem PVs have demonstrated the ability to outperform single-junction devices under diffuse light and non-standard spectra, highlighting their potential for superior field performance.

All-perovskite tandem flexible modules, combining high efficiency with mechanical adaptability, are well-suited for wearable electronics, curved surfaces, and building-integrated PVs (**Fig. 4d**). However, achieving long-term operational stability under mechanical stress, environmental exposure, and thermal cycling remains a formidable challenge (**Fig. 4e**). Studies have shown that replacing NiO_x with NiO_x/SAM transport layers significantly enhances mechanical resilience[77]. Further progress will require optimizing intermediate TRJ structures to balance electrical performance with bending flexibility, as well as mitigating delamination and thermal effects induced by laser scribing. For instance, bending-induced metal delamination along P3 grooves remains a critical issue, increasing the risk of short circuits[149] (**Fig. 4f**). Addressing these limitations is essential for advancing the reliability and scalability of flexible tandem modules.

Environmental lifecycle enhancement

The environmental footprint of all-perovskite tandem solar cells is a critical consideration for their large-scale adoption. Future industrialization should prioritize transitioning to fully green solvent-based or evaporation-based fabrication methods. Encapsulation plays a dual role: it ensures long-term device stability and serves as a vital barrier against Pb leakage during operation. Current encapsulation techniques include single-layer coatings, such as UV-curable epoxy resin or silicone[150] (**Fig. 4g**), and multi-step hot pressing using thermoplastic polymers[151] (**Fig. 4h** and **4i**). Among these, multi-step hot pressing is widely employed in industrial settings due to its robust protective capabilities, though it necessitates further innovation to enhance efficiency and flexibility while minimizing efficiency losses during the heating process. Future advancements should focus on developing high-performance multilayer barrier films, advanced adhesive interfaces, and innovative flexible encapsulation designs.

Despite the many challenges that remain in realizing the full potential of all-perovskite multi-junction devices, the sustained effort and rapid progress in perovskite research offer a promising outlook. We strongly believe that all-perovskite tandems present the ultimate embodiment of perovskite technology, paving the way for the development of highly efficient and cost-effective thin-film modules, and ultimately driving their large-scale manufacturing and deployment.

Figure captions

Box 1: a, The classification of all-perovskite tandem devices into 2T and 4T configurations. **b,** Perovskite materials and working principles of 2T all-perovskite tandem solar cell. **c,** A schematic illustration of how ion doping modifies the bandgap and energy levels of perovskite materials. **d,** A comparison of the efficiency progress of 2T and 4T all-perovskite tandem solar cells against single-junction counterparts[1,7-41].

Fig.1| Strategies to enhance efficiency in WBG and NBG subcells. a, Statistical performance parameters of WBG and NBG perovskite sub-cells in tandem configuration[9,10-14,16,18,22-25,48,55]. **b,** Sources of performance losses in p-i-n architecture of PSCs. **c,** Non-radiative recombination pathways in devices. Black circles with plus/minus signs represent holes and electrons. Horizontal dashed lines indicate split Fermi levels. Staggered short lines denote non-radiative recombination centers. Orange, blue, and purple arrowheads indicate non-radiative pathways at the HTL interface, perovskite bulk, and ETL interface, respectively. **d,** The issue of Sn^{2+} oxidized to Sn^{4+} by losing two electrons in NBG films. **e,** Photographs showing the ease of oxidation of Sn^{2+} to Sn^{4+} in ambient air and the facile reduction of Sn^{4+} to Sn^{2+} by metallic Sn powders. **f,** Schematic diagram of perovskite bulk crystallization regulation and grain boundary passivation. **g,** Cross-section scanning electron microscope (SEM) images of WBG perovskite films made with antisolvent and gas-quench methods. **h,** Schematic diagram of molecular passivation on the perovskite surface. **i,** Kelvin probe force microscopy (KPFM) images of control and PDA-treated WBG films. **j,** Schematic diagram of heterojunction formation at the perovskite interface. **k,** Cross-sectional high-resolution scanning transmission electron microscopy (HR-STEM) image and corresponding energy-dispersive X-ray (EDX) mapping of Pb-Sn PSCs with bilayer perovskite heterojunction. **l,** Schematic diagram of HTL improvement and buried passivation anchoring in devices. **m,** KPFM images of different NBG perovskite films deposited on PEDOT:PSS and MPA2FPh-BT-BA (2F). **e,** ref. [24], Springer Nature Limited; **g,** ref. [11], AAAS; **i,** ref. [10], Springer Nature Limited; **k,** ref. [14], Springer Nature Limited; **m,** ref. [13], Springer Nature Limited.

Fig. 2| Operational stability of subcells and tandem PVs. a, The stability issues of WBG perovskites. **b,** The summarized MPP statistics of WBG subcells[11,55,88–98]. **c,** The MPP stability of WBG solar cells with A site and X site alloying. The inset shows the effect of A-site and X-site ion engineering on the stability of WBG perovskite films. **d,** The summarized stability issues of NBG perovskites. **e,** The summarized MPP statistics of NBG subcells[9,48,71,98,102–111]. **f,** The MPP stability of NBG solar cells with P3CT HTL. The inset shows the calculated pKa values of functional groups attached to the methyl group in P3CT. **g,** The stability issues of all-perovskite tandem solar cells originating from TRJ. **h,** The summarized MPP statistics of all-perovskite solar cells with different TRJ[9,14,25,36,70,84,118–121]. **i,** The MPP stability of the art-of-the-state all-perovskite tandem solar cells with a TRJ structure of SnO_2/NC-ITO/SAMs. The inset shows a schematic diagram of bonding between SAMs and ITO or ITO NCs. **c,** ref. [55], Wiley-VCH; **f,** ref. [118], Cell Press; **i,** ref. [121], Wiley-VCH.

Fig.3| Upscaling fabrication of all-perovskite tandem. a, Illustration of upscaling from small-area (<1 cm^2, spin coating) to large-area (~1 cm^2, spin coating, blade coating, or fully scalable processing) and module dimension (>10 cm^2, fully scalable processing). **b**, PCE evolution of ~1 cm^2 all-perovskite PSCs[9,14,16,24,25,70,84,119,125,130] and min-modules[42,43,126–128,131,132]. **c**, Schematic illustration of all-perovskite solar modules with series interconnection and summarized possibilities of geometrical losses in module designs. **d**, Schematic illustration of scalable processing of large-area perovskite films and key control of crystallization. **e**, PCE progress of single-junction and all-perovskite tandem PSCs or modules based on blade-coating process[42,43,97,126–128,131–138]. **f**, Schematic of typical crystallization problems and mitigation strategies in large-area perovskite fabrication.

Fig.4| Prospect of all-perovskite tandem PV. a, Theoretical efficiency limits of multi-junction solar cells on the despondence of the number of subcells in combination with optimum bandgaps (data derived from Ref[141]. based on the detailed balance limits). **b,** Schematic illustration of energy harvesting in a bifacial tandem device, including direct sunlight, diffused light due to cloud cover, and reflected sunlight from the surrounding environment. **c,** EQE curves of WBG and NBG subcells in bifacial all-perovskite tandems with various top-cell bandgaps under front (glass) side illumination. **d,** Schematic illustration of bending test for a flexible module under bending. **e,** Schematic of mechanical fracture and delamination in a flexible tandem module after bending tests. **f,** Schematic of metal delamination at the P3 region in a flexible tandem module after bending tests. **g,** Photo of one-step coating polydimethylsiloxane-encapsulated device. **h,** Photos of ethylene-vinyl acetate encapsulated (left) and shellac-encapsulated (right) perovskite modules after hail impact testing. **i,** Schematic diagram of perovskite device encapsulation. **c,** ref. [148], Springer Nature Limited; **g,** ref. [150], Elsevier; **h,** ref. [151], Cell Press.

References

1. Green, M.A. et al. Solar Cell Efficiency Tables (Version 65). *Prog. Photovoltaics Res. Appl.* **33**, 3–15 (2025).
2. Aydin, E. *et al.* Pathways toward commercial perovskite/silicon tandem photovoltaics. *Science.* **383**, eadh3849 (2024).
3. Marti, A. & Araújo, G.L. Limiting efficiencies for photovoltaic energy conversion in multigap systems. *Sol. Energy Mater. Sol. Cells.* **43**, 203–222 (1996).
4. Ko, Y., Park, H., Lee, C., Kang, Y. & Jun, Y. Recent Progress in Interconnection Layer for Hybrid Photovoltaic Tandems. *Adv. Mater.* **32**, 2002196 (2020).
5. Brivio, F., Walker, A.B. & Walsh, A. Structural and electronic properties of hybrid perovskites for high-efficiency thin-film photovoltaics from first-principles. *APL Mater.* **1**, 042111 (2013).
6. Walsh, A. Principles of chemical bonding and band gap engineering in hybrid organic-inorganic halide perovskites. *J. Phys. Chem. C* **119**, 5755–5760 (2015).
7. Heo, J.H. & Im, S.H. $CH_3NH_3PbBr_3$–$CH_3NH_3PbI_3$Perovskite–Perovskite Tandem Solar Cells with Exceeding 2.2 V Open Circuit Voltage. *Adv. Mater.* **28**, 5121–5125 (2016).
8. Eperon, G.E. et al. Perovskite-perovskite tandem photovoltaics with optimized band gaps. *Science.* **354**, 861–865 (2016).

   The first report on fabricating all-perovskite tandems using ideally bandgap-matched subcells.
9. Lin, R. et al. All-perovskite tandem solar cells with improved grain surface passivation. *Nature.* **603**, 73–78 (2022).

   This is the first demonstration of all-perovskite tandem solar cells outperforming the highest-efficiency single-junction counterparts.
10. Chen, H. et al. Regulating surface potential maximizes voltage in all-perovskite tandems. *Nature.* **613**, 676–681 (2023).
11. Jiang, Q. et al. Compositional texture engineering for highly stable wide-bandgap perovskite solar cells. *Science.* **378**, 1295–1300 (2022).

    This work advances wide-bandgap subcell performance and achieves the longest reported stability of all-perovskite tandem solar cells.
12. Zhou, S. et al. Aspartate all-in-one doping strategy enables efficient all-perovskite tandems. *Nature.* **624**, 69–73 (2023).
13. Zhu, J. et al. A donor–acceptor-type hole-selective contact reducing non-radiative recombination losses in both subcells towards efficient all-perovskite tandems. *Nat. Energy* **8**, 714–724 (2023).
14. Lin, R. et al. All-perovskite tandem solar cells with 3D/3D bilayer perovskite heterojunction. *Nature.* **620**, 994–1000 (2023).

15. Yu, D. et al. Electron-withdrawing organic ligand for high-efficiency all-perovskite tandem solar cells. *Nat. Energy.* **9**, 298–307 (2024).

16. Li, C. et al. Diamine chelates for increased stability in mixed Sn–Pb and all-perovskite tandem solar cells. *Nat. Energy.* **9**, 1388–1396 (2024).

17. Pan, Y. et al. Surface chemical polishing and passivation minimize non-radiative recombination for all-perovskite tandem solar cells. *Nat. Commun.* **15**, 7335 (2024).

18. Liu, Z. et al. All-perovskite tandem solar cells achieving >29% efficiency with improved (100) orientation in wide-bandgap perovskites. *Nat. Mater.* **24**, 252–259 (2025).

19. Forgács, D. et al. Efficient Monolithic Perovskite/Perovskite Tandem Solar Cells. *Adv. Energy Mater.* **7**, 1602121 (2017).

20. Rajagopal, A. et al. Highly Efficient Perovskite–Perovskite Tandem Solar Cells Reaching 80% of the Theoretical Limit in Photovoltage. *Adv. Mater.* **29**, 1702140 (2017).

21. Leijtens, T. et al. Tin-lead halide perovskites with improved thermal and air stability for efficient all-perovskite tandem solar cells. *Sustain. Energy Fuels* **2**, 2450–2459 (2018).

22. Zhao, D. et al. Efficient two-terminal all-perovskite tandem solar cells enabled by high-quality low-bandgap absorber layers. *Nat. Energy.* **3**, 1093–1100 (2018).

23. Tong, J. et al. Carrier lifetimes of >1 ms in Sn-Pb perovskites enable efficient all-perovskite tandem solar cells. *Science.* **364**, 475–479 (2019).

24. Lin, R. et al. Monolithic all-perovskite tandem solar cells with 24.8% efficiency exploiting comproportionation to suppress Sn(ii) oxidation in precursor ink. *Nat. Energy.* **4**, 864–873 (2019).

This work demonstrates, for the first time, a narrow-bandgap subcell exceeding 21% efficiency, accompanied by the design of a key tunnel junction structure.

25. Xiao, K. et al. All-perovskite tandem solar cells with 24.2% certified efficiency and area over 1 cm2 using surface-anchoring zwitterionic antioxidant. *Nat. Energy.* **5**, 870–880 (2020).

26. Gao, H. et al. Thermally Stable All-Perovskite Tandem Solar Cells Fully Using Metal Oxide Charge Transport Layers and Tunnel Junction. *Sol. RRL.* **5**, 2100814 (2021).

27. Zhou, H. et al. Interface engineering of highly efficient perovskite solar cells. *Science.* **345**, 542–546 (2014).

28. Jeon, N.J. et al. Compositional engineering of perovskite materials for high-performance solar cells. *Nature* **517**, 476–480 (2015).

29. Yang, W.S. et al. Iodide management in formamidinium-lead-halide–based perovskite layers for efficient solar cells. *Science.* **356**, 1376–1379 (2017).

30. Jiang, Q. et al. Surface passivation of perovskite film for efficient solar cells. *Nat. Photonics* **13**, 460–466 (2019).

31. Jeong, J. *et al.* Pseudo-halide anion engineering for α-$FAPbI_3$ perovskite solar cells. *Nature.* **592**, 381–385 (2021).

32. Yoo, J.J. et al. Efficient perovskite solar cells via improved carrier management. *Nature.* **590**, 587–593 (2021).

33. Min, H. et al. Perovskite solar cells with atomically coherent interlayers on SnO2 electrodes. *Nature.* **598**, 444–450 (2021).

34. Park, J. et al. Controlled growth of perovskite layers with volatile alkylammonium chlorides. *Nature.* **616**, 724–730 (2023).

35. Chen, H. et al. Improved charge extraction in inverted perovskite solar cells with dual-site-binding ligands. *Science.* **193**, 189–193 (2024).

36. Wang, C. et al. A universal close-space annealing strategy towards high-quality perovskite absorbers enabling efficient all-perovskite tandem solar cells. *Nat. Energy.* **7**, 744–753 (2022).

37. Zhao, D. et al. Low-bandgap mixed tin–lead iodide perovskite absorbers with long carrier lifetimes for all-perovskite tandem solar cells. *Nat. Energy.* **2**, 17018 (2017).

38. Moradbeigi, M. & Razaghi, M. Investigation of optical and electrical properties of novel 4T all perovskite tandem solar cell. *Sci. Rep.* **12**, 6733 (2022).

39. Zeng, G. et al. Trapping Tetravalent Tin and Protecting Stannous in Tin-Lead Mixed Perovskites for Efficient All-Perovskite Tandem Solar Cells. *Adv. Funct. Mater.* **35**, 4048–4058 (2025).

40. Li, G. et al. Boosting All-Perovskite Tandem Solar Cells by Revitalizing the Buried Tin-Lead Perovskite Interface. *Adv. Mater.* **36**, 2401698 (2024).

41. Guan, H. et al. Efficient 1.77 eV-bandgap perovskite and all-perovskite tandem solar cells enabled by long-alkyl phosphonic acid. *Energy Environ. Sci.* **17**, 8219–8227 (2024).

42. Xiao, K. et al. Scalable processing for realizing 21.7%-efficient all-perovskite tandem solar modules. *Science.* **376**, 762–767 (2022).

This work reports the first all blade-coated all-perovskite tandem mini-module.

43. Gao, H. et al. Homogeneous crystallization and buried interface passivation for perovskite tandem solar modules. *Science.* **383**, 855–859 (2024).

44. Chung, I. et al. $CsSnI_3$: semiconductor or metal? High electrical conductivity and strong near-infrared photoluminescence from a single material. High hole mobility and phase-transitions. *J. Am. Chem. Soc.* **134**, 8579–8587 (2012).

45. Wang, D. et al. All-In-One Additive Enabled Efficient and Stable Narrow-Bandgap Perovskites for Monolithic All-Perovskite Tandem Solar Cells. *Adv. Mater.* **36**, 2411677 (2024).

46. Yang, M. et al. Sn-Pb Perovskite with Strong Light and Oxygen Stability for All-Perovskite Tandem Solar Cells. *Adv. Mater.* **37**, 2415627 (2025).

47. Yang, Z. et al. Enhancing electron diffusion length in narrow-bandgap perovskites for efficient monolithic perovskite tandem solar cells. *Nat. Commun.* **10**, 4498 (2019).

48. Tong, J. et al. Carrier control in Sn–Pb perovskites via 2D cation engineering for all-perovskite tandem solar cells with improved efficiency and stability. *Nat. Energy.* **7**, 642–651 (2022).

49. Oliver, R.D.J. et al. Understanding and suppressing non-radiative losses in methylammonium-free wide-bandgap perovskite solar cells. *Energy Environ. Sci.* **15**, 714–726 (2022).

50. Mahesh, S. *et al.* Revealing the origin of voltage loss in mixed-halide perovskite solar cells. *Energy Environ. Sci.* **13**, 258–267 (2020).

51. Stolterfoht, M. et al. How To Quantify the Efficiency Potential of Neat Perovskite Films: Perovskite Semiconductors with an Implied Efficiency Exceeding 28%. *Adv. Mater.* **32**, 2000080 (2020).

52. Hörantner, M. T. & Snaith, H. J. Predicting and optimising the energy yield of perovskite-on-silicon tandem solar cells under real world conditions. *Energy Environ. Sci.* **10**, 1983–1993 (2017).

53. Macpherson, S. et al. Local nanoscale phase impurities are degradation sites in halide perovskites. *Nature.* **607**, 294–300 (2022).

54. Frohna, K. et al. The impact of interfacial quality and nanoscale performance disorder on the stability of alloyed perovskite solar cells. *Nat. Energy.* **10**, 66–76 (2024).

55. Wen, J. et al. Steric Engineering Enables Efficient and Photostable Wide-Bandgap Perovskites for All-Perovskite Tandem Solar Cells. *Adv. Mater.* **34**, 2110356 (2022).

56. Ternes, S., Laufer, F. & Paetzold, U. W. Modeling and Fundamental Dynamics of Vacuum, Gas, and Antisolvent Quenching for Scalable Perovskite Processes. *Adv. Sci.* **11**, 2308901 (2024).

57. Wu, Z. et al. Enhancing Photovoltaically Preferred Orientation in Wide-Bandgap Perovskite for Efficient All-Perovskite Tandem Solar Cells. *Adv. Mater.* **37**, 202412943 (2025).

58. Isikgor, F.H. et al. Molecular engineering of contact interfaces for high-performance perovskite solar cells. *Nat. Rev. Mater.* **8**, 89–108 (2022).

59. Yang, G. et al. Stable and low-photovoltage-loss perovskite solar cells by multifunctional passivation. *Nat. Photonics.* **15**, 681–689 (2021).

60. Caprioglio, P. et al. Open-circuit and short-circuit loss management in wide-gap perovskite p-i-n solar cells. *Nat. Commun.* **14**, 932 (2023).

61. Liu, Z. et al. Reducing perovskite/C_{60} interface losses via sequential interface engineering for efficient perovskite/silicon tandem solar cell. *Adv. Mater.* **36**, 2308370 (2024).

62. Wang, X. et al. Highly efficient perovskite/organic tandem solar cells enabled by mixed-cation surface modulation. *Adv. Mater.* **35**, 2305946 (2023).

63. Liu, C. et al. Bimolecularly passivated interface enables efficient and stable inverted perovskite solar cells. *Science.* **382**, 810–815 (2023).

64. Sun, R. et al. An Orientation-Enhanced Interlayer Enables Efficient Sn–Pb Binary Perovskite Solar Cells and All-Perovskite Tandem Solar Cells with High Fill Factors. *Nano Lett.* **25**, 138–146 (2025).

65. Liu, J. et al. Efficient and stable perovskite-silicon tandem solar cells through contact displacement by MgF_x. *Science.* **377**, 302–306 (2022).

66. Yang, X. et al. Buried Interfaces in Halide Perovskite Photovoltaics. *Adv. Mater.* **33**, 2006435 (2021).

67. Xiao, T. et al. Elimination of grain surface concavities for improved perovskite thin-film interfaces. *Nat. Energy.* **9**, 999–1010 (2024).

68. Zhu, J. et al. Self-assembled hole-selective contact for efficient Sn-Pb perovskite solar cells and all-perovskite tandems. *Nat. Commun.* **16**, 240 (2025).

69. Al-Ashouri, A. et al. Monolithic perovskite/silicon tandem solar cell with >29% efficiency by enhanced hole extraction. *Science.* **370**, 1300–1309 (2020).

This work broadens the use of self-assembled monolayers in wide-bandgap subcells, offering important insights for inverted perovskite architectures.

70. He, R. et al. Improving interface quality for 1-cm^2 all-perovskite tandem solar cells. *Nature* **618**, 80–86 (2023).

71. Hu, S. et al. Optimized carrier extraction at interfaces for 23.6% efficient tin–lead perovskite solar cells. *Energy Environ. Sci.* **15**, 2096–2107 (2022).

72. Wang, J. et al. Halide homogenization for low energy loss in 2-eV-bandgap perovskites and increased efficiency in all-perovskite triple-junction solar cells. *Nat. Energy.* **9**, 70–80 (2023).

73. Hoke, E.T. et al. Reversible photo-induced trap formation in mixed-halide hybrid perovskites for photovoltaics. *Chem. Sci.* **6**, 613–617 (2015).

74. Barker, A.J. et al. Defect-Assisted Photoinduced Halide Segregation in Mixed-Halide Perovskite Thin Films. *ACS Energy Lett.* **2**, 1416–1424 (2017).

75. Beal, R.E. et al. Structural Origins of Light-Induced Phase Segregation in Organic-Inorganic Halide Perovskite Photovoltaic Materials. *Matter.* **2**, 207–219 (2020).

76. Mcmeekin, D.P. et al. A mixed-cation lead mixed-halide perovskite absorber for tandem solar cells. *Science.* **351**, 151–156 (2016).

77. Palmstrom, A. F. et al. Enabling Flexible All-Perovskite Tandem Solar Cells. *Joule.* **3**, 2193–2204 (2019).

78. Huang, Z. et al. Stable, Bromine-Free, Tetragonal Perovskites with 1.7 eV Bandgaps via A-Site Cation Substitution. *ACS Mater. Lett.* **2**, 869–872 (2020).

79. Xu, J. et al. Triple-halide wide-band gap perovskites with suppressed phase segregation for efficient tandems. *Science.* **367**, 1097–1104 (2020).

80. Tang, X. et al. Local Observation of Phase Segregation in Mixed-Halide Perovskite. *Nano Lett.* **18**, 2172–2178 (2018).

81. Ahn, N. et al. Trapped charge-driven degradation of perovskite solar cells. *Nat. Commun.* **7**, 13422 (2016).

82. Khenkin, M.V., Anoop, K.M., Katz, E.A. & Visoly-Fisher, I. Bias-dependent degradation of various solar cells: Lessons for stability of perovskite photovoltaics. *Energy Environ. Sci.* **12**, 550–558 (2019).

83. Lin, Y. et al. Excess charge-carrier induced instability of hybrid perovskites. *Nat. Commun.* **9**, 4981 (2018).

84. Wen, J. et al. Heterojunction formed via 3D-to-2D perovskite conversion for photostable wide-bandgap perovskite solar cells. *Nat. Commun.* **14**, 7118 (2023).

85. Park, S. M. et al. Low-loss contacts on textured substrates for inverted perovskite solar cells. *Nature* **624**, 289–294 (2023).

86. Tang, H. et al. Reinforcing self-assembly of hole transport molecules for stable inverted perovskite solar cells. *Science.* **383**, 1236–1240 (2024).

87. Elnaggar, M. et al. Decoupling Contributions of Charge-Transport Interlayers to Light-Induced Degradation of p-i-n Perovskite Solar Cells. *Sol. RRL.* **4**, 2000191 (2020).

88. Liu, L. et al. Self-Assembled Amphiphilic Monolayer for Efficient and Stable Wide-Bandgap Perovskite Solar Cells. *Adv. Energy Mater.* **13**, 2202802 (2023).

89. Wang, R. et al. Efficient wide-bandgap perovskite photovoltaics with homogeneous halogen-phase distribution. *Nat. Commun.* **15**, 8899 (2024).

90. Xie, Y. et al. Homogeneous grain boundary passivation in wide-bandgap perovskite films enables fabrication of monolithic perovskite/organic tandem solar cells with over 21% efficiency. *Adv. Funct. Mater.* **32**, 2112126 (2022).

91. Susic, I., Gil-Escrig, L., Palazon, F., Sessolo, M. & Bolink, H.J. Quadruple-cation wide-bandgap perovskite solar cells with enhanced thermal stability enabled by vacuum deposition. *ACS Energy Lett.* **7**, 1355–1363 (2022).

92. Li, T. et al. Inorganic wide-bandgap perovskite subcells with dipole bridge for all-perovskite tandems. *Nat. Energy.* **8**, 610–620 (2023).

93. Wang, C. et al. Suppressing phase segregation in wide bandgap perovskites for monolithic perovskite/organic tandem solar cells with reduced voltage loss. *Small.* **18**, 2204081 (2022).

94. Shen, X. et al. Chloride-Based Additive Engineering for Efficient and Stable Wide-Bandgap Perovskite Solar Cells. *Adv. Mater.* **35**, 2211742 (2023).

95. Zhang, Z. et al. Organizing Uniform Phase Distribution in Methylammonium-Free 1.77 eV Wide-Bandgap Inverted Perovskite Solar Cells. *Small.* **19**, 2303213 (2023).

96. Guo, X. et al. Stabilizing efficient wide-bandgap perovskite in perovskite-organic tandem solar cells. *Joule.* **8**, 2554–2569 (2024).

97. Fang, H. et al. Efficient Blade-Coated Wide-Bandgap and Tandem Perovskite Solar Cells via a Three-Step Restraining Strategy. *Adv. Mater.* **37**, 2414790 (2025).

98. Tzoganakis, N., Spiliarotis, E., Tsikritzis, D. & Kymakis, E. 4F-Phenethylammonium chloride as a key component for interfacial engineering of wide-bandgap perovskite absorber. *Nano Energy.* **128**, 109914 (2024).

99. Azmi, R. et al. Damp heat–stable perovskite solar cells with tailored-dimensionality 2D/3D heterojunctions. *Science.* **376**, 73–77 (2022).

100. Chen, H. et al. Quantum-size-tuned heterostructures enable efficient and stable inverted perovskite solar cells. *Nat. Photonics.* **31**, 1903559 (2022).

101. Choi, H. et al. A Review on Reducing Grain Boundaries and Morphological Improvement of Perovskite Solar Cells from Methodology and Material-Based Perspectives. *Small Methods.* **4**, 1900569 (2020).

102. Chen, B. et al. Bifacial all-perovskite tandem solar cells. *Sci. Adv.* **8**, eadd0377 (2022).

103. Sun, Q. et al. Surface charge transfer doping of narrow-bandgap Sn–Pb perovskites for high-performance tandem solar cells. *Energy Environ. Sci.* **17**, 2512–2520 (2024).

104. Wang, J. et al. Enhancing photostability of Sn-Pb perovskite solar cells by an alkylammonium pseudo-halogen additive. *Adv. Energy Mater.* **13**, 2204115 (2023).

105. Wang, M. et al. Ammonium cations with high p K a in perovskite solar cells for improved high-temperature photostability. *Nat. Energy.* **8**, 1229–1239 (2023).

106. Zhou, Y. et al. Defect-less formamidinium Sn–Pb perovskite grown on a fluorinated substrate with top-down crystallization control for efficient and stable photovoltaics. *Energy Environ. Sci.* **17**, 2845–2855 (2024).

107. Wu, P. et al. Efficient and Thermally Stable All-Perovskite Tandem Solar Cells Using All-FA Narrow-Bandgap Perovskite and Metal-oxide-based Tunnel Junction. *Adv. Energy Mater.* **12**, 2202948 (2022).

108. Tan, S. et al. Sustainable thermal regulation improves stability and efficiency in all-perovskite tandem solar cells. *Nat. Commun.* **15**, 4136 (2024).

109. Lin, Z. et al. Self-assembly construction of a homojunction of Sn–Pb perovskite using an antioxidant for all-perovskite tandem solar cells with improved efficiency and stability. *Energy Environ. Sci.* **17**, 6314–6322 (2024).

110. Yu, Z. et al. Solution-processed ternary tin (II) alloy as hole-transport layer of Sn–Pb perovskite solar cells for enhanced efficiency and stability. *Adv. Mater.* **34**, 2205769 (2022).

111. Lee, S. et al. Unprecedented inorganic HTL-based MA-free Sn–Pb perovskite photovoltaics with an efficiency over 23%. *Energy Environ. Sci.* **17**, 8140–8150 (2024).

112. Alsulami, A. et al. Triiodide Formation Governs Oxidation Mechanism of Tin-Lead Perovskite Solar Cells via A-Site Choice. *J. Am. Chem. Soc.* **146**, 22970–22981 (2024).

113. Zhang, Y. et al. Synchronized crystallization in tin-lead perovskite solar cells. *Nat. Commun.* **15**, 6887 (2024).

114. Duan, C. et al. Durable all-inorganic perovskite tandem photovoltaics. *Nature.* **637**, 1111–1117 (2025).

115. He, D. et al. Synergistic Passivation of Buried Interface and Grain Boundary of Tin–Lead Mixed Perovskite Films for Efficient Solar Cells. *Adv. Funct. Mater.* **34**, 2411750 (2024).

116. Song, J. et al. Multifunctional Ammonium Sulfide Enables Highest Efficiency Lead–Tin Perovskite Solar Cells. *Adv. Funct. Mater.* **35**, 202411746 (2025).

117. Zhu, J. et al. Custom-tailored hole transport layer using oxalic acid for high-quality tin-lead perovskites and efficient all-perovskite tandems. *Sci. Adv.* **10**, eadl2063 (2024).

118. Fu, S. et al. Suppressed deprotonation enables a durable buried interface in tin-lead perovskite for all-perovskite tandem solar cells. *Joule.* **8**, 2220–2237 (2024).

119. Yu, Z. et al. Simplified interconnection structure based on C_{60}/SnO_{2-x} for all-perovskite tandem solar cells. *Nat. Energy.* **5**, 657–665 (2020).

120. Wang, Y. et al. Oxidation-resistant all-perovskite tandem solar cells in substrate configuration. *Nat. Commun.* **14**, 1819 (2023).

121. Liu, C. et al. Efficient All-Perovskite Tandem Solar Cells with Low-Optical-Loss Carbazolyl Interconnecting Layers. *Angew. Chemie.* **135**, e202313374 (2023).

122. Chen, W. et al. Monolithic perovskite/organic tandem solar cells with 23.6% efficiency enabled by reduced voltage losses and optimized interconnecting layer. *Nat. Energy.* **7**, 229–237 (2022).

123. Brinkmann, K.O. et al. Perovskite–organic tandem solar cells with indium oxide interconnect. *Nature.* **604**, 280–286 (2022).

124. Khenkin, M.V. et al. Consensus statement for stability assessment and reporting for perovskite photovoltaics based on ISOS procedures. *Nat. Energy.* **5**, 35–49 (2020).

125. Wang, Y. et al. Homogenized contact in all-perovskite tandems using tailored 2D perovskite. *Nature.* **635**, 867–873 (2024).

126. Dai, X. et al. Efficient monolithic all-perovskite tandem solar modules with small cell-to-module derate. *Nat. Energy.* **7**, 923–931 (2022).

127. Duan, C. et al. Scalable fabrication of wide-bandgap perovskites using green solvents for tandem solar cells. *Nat. Energy.* **10,** 318–328 (2025).

128. Abdollahi Nejand, B. et al. Scalable two-terminal all-perovskite tandem solar modules with a 19.1% efficiency. *Nat. Energy.* **7**, 620–630 (2022).

The first reported work on all-perovskite tandem modules.

129. Park, N. G. & Zhu, K. Scalable fabrication and coating methods for perovskite solar cells and solar modules. *Nat. Rev. Mater.* **5**, 333–350 (2020).

130. Li, L. et al. Flexible all-perovskite tandem solar cells approaching 25% efficiency with molecule-bridged hole-selective contact. *Nat. Energy.* **7**, 708–717 (2022).

This work presents the first report of flexible all-perovskite tandem solar cells.

131. Shi, Y. et al. High-Speed Deposition of Large-Area Narrow-Bandgap Perovskite Films for All-Perovskite Tandem Solar Mini-Modules. *Adv. Funct. Mater.* **33**, 2307209 (2023).

132. Sun, H. et al. Scalable Solution-Processed Hybrid Electron Transport Layers for Efficient All-Perovskite Tandem Solar Modules. *Adv. Mater.* **36**, 2308706 (2024).

133. Siegrist, S. et al. Stabilizing solution–substrate interaction of perovskite ink on PEDOT: PSS for scalable blade coated narrow bandgap perovskite solar modules by gas quenching. *Sol. RRL.* **8**, 2400447 (2024).

134. Zhou, X. et al. Suppressing Nonradiative Losses in Wide-Band-Gap Perovskites Affords Efficient and Printable All-Perovskite Tandem Solar Cells with a Metal-Free Charge Recombination Layer. *ACS Energy Lett.* **8**, 502–512 (2023).

135. Pu, D. et al. Enhancing Efficiency and Intrinsic Stability of Large-Area Blade-Coated Wide-Bandgap Perovskite Solar Cells Through Strain Release. *Adv. Funct. Mater.* **34**, 202314349 (2024).

136. Zeng, L. et al. 2D-3D heterostructure enables scalable coating of efficient low-bandgap Sn–Pb mixed perovskite solar cells. *Nano Energy.* **66**, 104099 (2019).

137. Li, C. et al. Vertically Aligned 2D/3D Pb–Sn Perovskites with Enhanced Charge Extraction and Suppressed Phase Segregation for Efficient Printable Solar Cells. *ACS Energy Lett.* **5**, 1386–1395 (2020).

138. Babu, V. et al. Toward up-scaling the four-terminal all-perovskite tandem solar modules on flexible substrates. *Mater. Today Energy* **28**, 101073 (2022).

139. Yin, M. et al. A Revisit of Crystallization in Tin Halide Perovskite Thin Films: From Nucleation, Intermediate to Crystal Growth. *Adv. Funct. Mater.* **34**, 2404792 (2024).

140. Hu, S. et al. Narrow Bandgap Metal Halide Perovskites for All-Perovskite Tandem Photovoltaics. *Chem. Rev.* **124**, 4079–4123 (2024).

141. Philipps, S.P. & Bett, A.W. III-V Multi-junction solar cells and concentrating photovoltaic (CPV) systems. *Adv. Opt. Technol.* **3**, 469–478 (2014).

142. Hörantner, M.T. et al. The Potential of Multijunction Perovskite Solar Cells. *ACS Energy Lett.* **2**, 2506–2513 (2017).

143. Hu, S. et al. Steering perovskite precursor solutions for multijunction photovoltaics. *Nature.* **639**, 93–101 (2025).

This work is the first to report the fabrication of four-junction all-perovskite tandem solar cells.

144. Liu, S. et al. Triple-junction solar cells with cyanate in ultrawide-bandgap perovskites. *Nature.* **628**, 306–312 (2024).

145. Wang, Z. et al. Suppressed phase segregation for triple-junction perovskite solar cells. *Nature.* **618**, 74–79 (2023).

146. Gao, Y. et al. Performance optimization of monolithic all-perovskite tandem solar cells under standard and real-world solar spectra. *Joule.* **6**, 1944–1963 (2022).

147. Gota, F., An, S. X., Hu, H., Abdollahi Nejand, B. & Paetzold, U.W. Energy Yield Modeling of Bifacial All-Perovskite Two-Terminal Tandem Photovoltaics. *Adv. Opt. Mater.* **11**, 2201691 (2023).

148. Li, H. et al. Revealing the output power potential of bifacial monolithic all-perovskite tandem solar cells. *eLight.* **2**, 21 (2022).

149. Xu, W. et al. Multifunctional entinostat enhances the mechanical robustness and efficiency of flexible perovskite solar cells and minimodules. *Nat. Photonics.* **18**, 379–387 (2024).

150. Mousavi, S.M. et al. Addressing the efficiency loss and degradation of triple cation perovskite solar cells via integrated light managing encapsulation. *Mater. Today Energy.* **46**, 101707 (2024).

151. Zhang, G. et al. Shellac protects perovskite solar cell modules under real-world conditions. *Joule.* **8**, 496–508 (2024).

Acknowledgment

H.T. and J.W. acknowledge financial support from the National Key R&D Program of China (2022YFB4200304), the National Natural Science Foundation of China (T2325016, U21A2076, 61974063, 62125402, 62321166653, 62305150), the Natural Science Foundation of Jiangsu Province (BE2022021, BE2022026, BK20202008, BK20190315, BK20232022), the Fundamental Research Funds for the Central Universities (0213/14380206, 0205/14380252), the Frontiers Science Center for Critical Earth Material Cycling Fund (DLTD2109), the "GeoX" Interdisciplinary Research Funds for the Frontiers Science Center for Critical Earth Material Cycling at Nanjing University, and the Program for Innovative Talents and Entrepreneurs in Jiangsu. H.H. and U.W.P. acknowledge funding partly provided by the European Union (ERC Consolidator Grant, Lami-Pero, 101087673). Views and opinions expressed are, however, those of the authors only and do not necessarily reflect those of the European Union or the European Research Council Executive Agency. Neither the European Union nor the granting authority can be held responsible for them. C.C. acknowledges support from the Innovation Project of Optics Valley Laboratory (OVL2024ZD002). D.P.M. and H.J.S. are funded by the European Union. Views and opinions expressed are, however, those of the author(s) only and do not necessarily reflect those of the European Union or the Research and Innovation Agency (RIA). Neither the European Union nor the granting authority can be held responsible for them. The NEXUS project has received funding from the European Union's Horizon Europe research and innovation program under grant agreement No. 101075330. Additional support is acknowledged from the program grants funded by the Engineering and Physical Science Research Council (EPSRC), including ATIP (EP/T028513/1) and HEFSPV (EP/V027131/1).

Competing interests

Hairen Tan is the founder, Chief Scientific Officer, and Chairman of Renshine Solar Co., Ltd., a company that is commercializing perovskite PVs. H.J.S. is the co-founder and CSO of Oxford PV Ltd. The other authors declare no competing financial or non-financial interests.

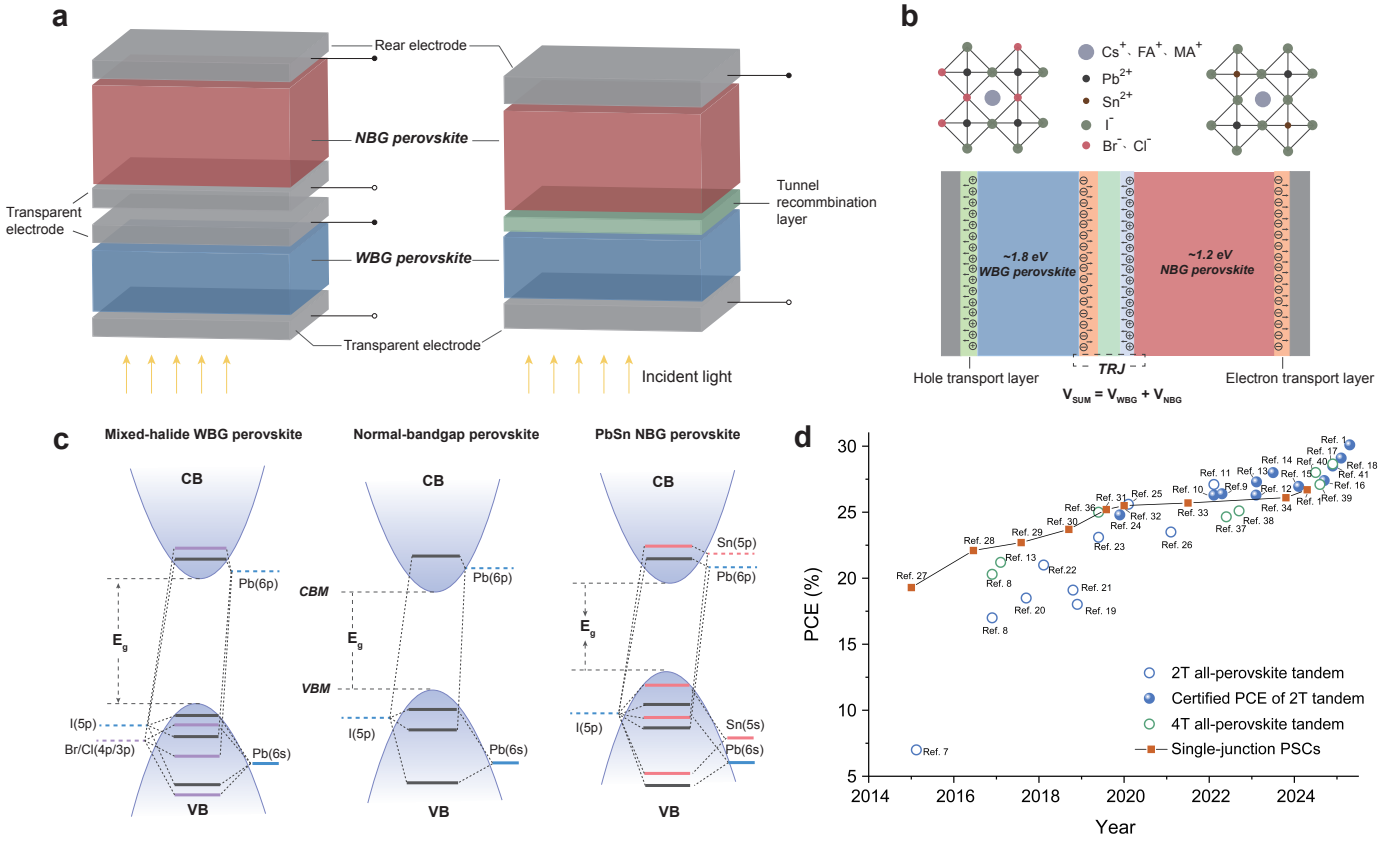
a
Rear electrode
NBG perovskite
Transparent electrode
WBG perovskite
Transparent electrode
Tunnel recommbination layer
Incident light
b
Cs+、FA+、MA+
Pb2+
Sn2+
I-
Br-、Cl-
~1.8 eV WBG perovskite
~1.2 eV NBG perovskite
TRJ
Hole transport layer
Electron transport layer
V_SUM = V_WBG + V_NBG
c
Mixed-halide WBG perovskite
Normal-bandgap perovskite
PbSn NBG perovskite
CB
VB
Pb(6p)
Pb(6s)
Sn(5p)
Sn(5s)
E_g
CBM
VBM
I(5p)
Br/Cl(4p/3p)
d
PCE (%)
Year
2T all-perovskite tandem
Certified PCE of 2T tandem
4T all-perovskite tandem
Single-junction PSCs

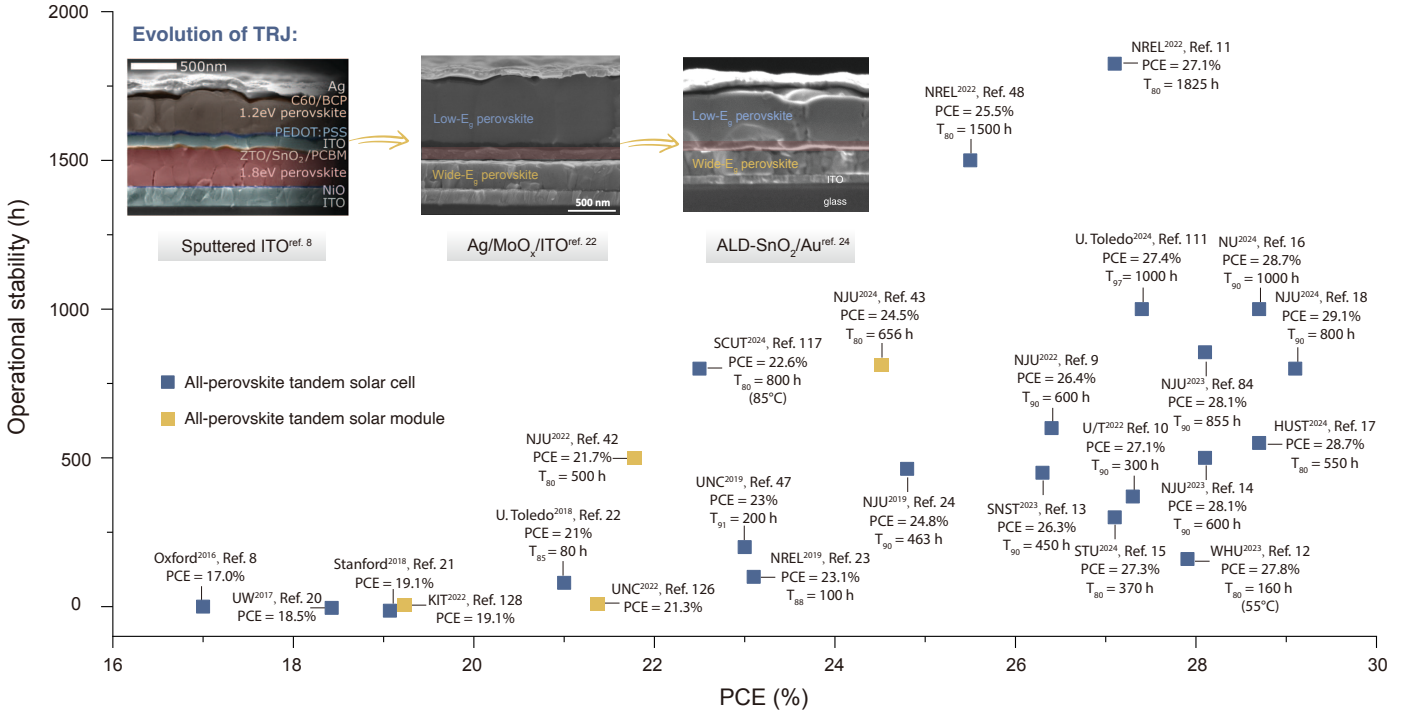
Evolution of TRJ:
500nm
Ag
C60/BCP
1.2eV perovskite
PEDOT:PSS
ITO
ZTO/SnO2/PCBM
1.8eV perovskite
NiO
ITO
Low-Eg perovskite
Wide-Eg perovskite
500 nm
Low-Eg perovskite
Wide-Eg perovskite
ITO
glass
Sputtered ITOref. 8
Ag/MoOx/ITOref. 22
ALD-SnO2/Auref. 24
Operational stability (h)
PCE (%)
All-perovskite tandem solar cell
All-perovskite tandem solar module
2000
1500
1000
500
0
16
18
20
22
24
26
28
30
Oxford2016, Ref. 8
PCE = 17.0%
UW2017, Ref. 20
PCE = 18.5%
Stanford2018, Ref. 21
PCE = 19.1%
KIT2022, Ref. 128
PCE = 19.1%
U. Toledo2018, Ref. 22
PCE = 21%
T85 = 80 h
NJU2022, Ref. 42
PCE = 21.7%
T80 = 500 h
UNC2022, Ref. 126
PCE = 21.3%
UNC2019, Ref. 47
PCE = 23%
T91 = 200 h
NREL2019, Ref. 23
PCE = 23.1%
T88 = 100 h
SCUT2024, Ref. 117
PCE = 22.6%
T80 = 800 h
(85°C)
NJU2024, Ref. 43
PCE = 24.5%
T80 = 656 h
NJU2019, Ref. 24
PCE = 24.8%
T90 = 463 h
NREL2022, Ref. 48
PCE = 25.5%
T80 = 1500 h
NREL2022, Ref. 11
PCE = 27.1%
T80 = 1825 h
U. Toledo2024, Ref. 111
PCE = 27.4%
T97 = 1000 h
NU2024, Ref. 16
PCE = 28.7%
T90 = 1000 h
NJU2024, Ref. 18
PCE = 29.1%
T90 = 800 h
NJU2022, Ref. 9
PCE = 26.4%
T90 = 600 h
NJU2023, Ref. 84
PCE = 28.1%
T90 = 855 h
U/T2022 Ref. 10
PCE = 27.1%
T90 = 300 h
HUST2024, Ref. 17
PCE = 28.7%
T80 = 550 h
SNST2023, Ref. 13
PCE = 26.3%
T90 = 450 h
NJU2023, Ref. 14
PCE = 28.1%
T90 = 600 h
STU2024, Ref. 15
PCE = 27.3%
T80 = 370 h
WHU2023, Ref. 12
PCE = 27.8%
T80 = 160 h
(55°C)

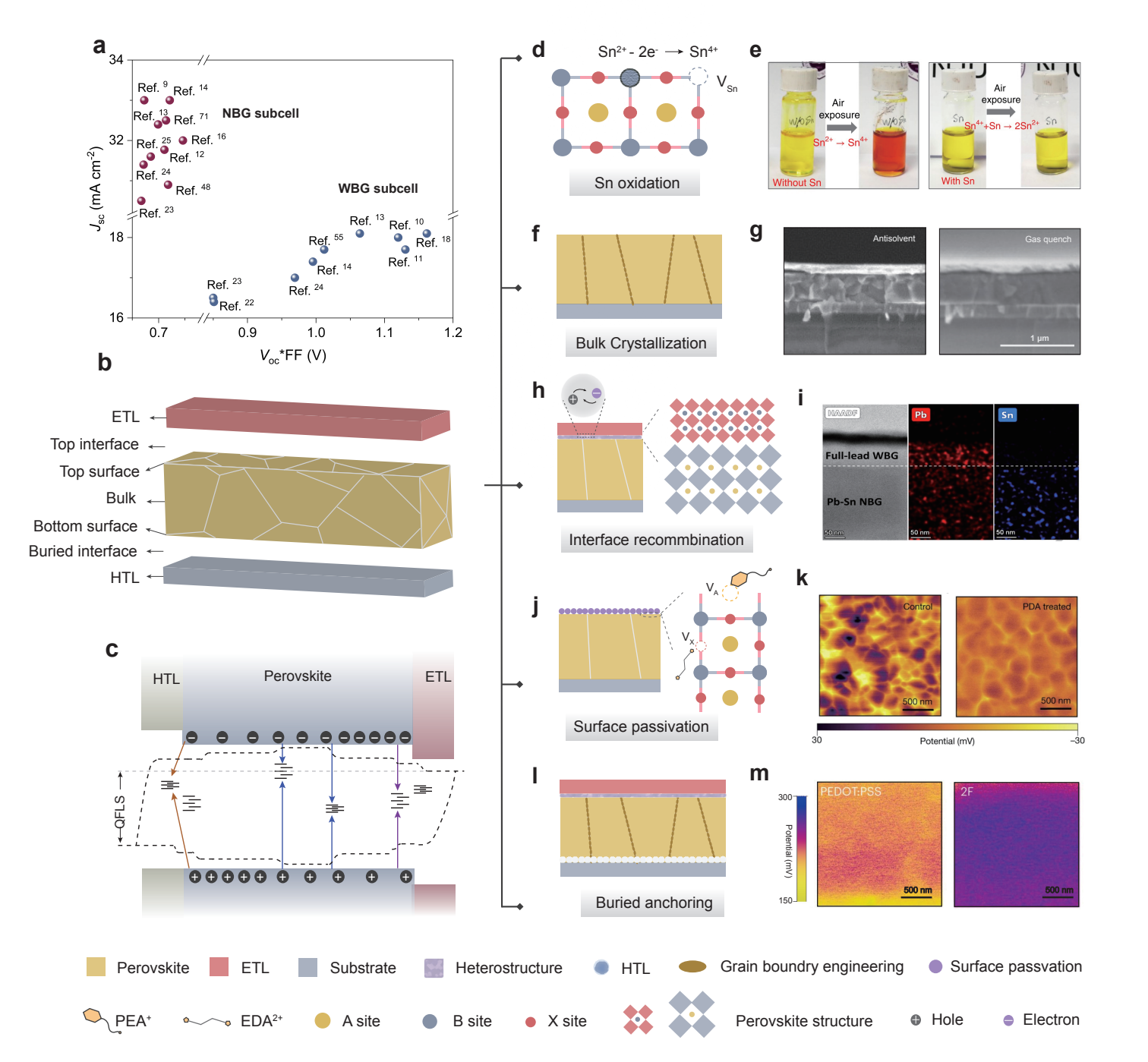
a
NBG subcell
WBG subcell
Ref. 9
Ref. 14
Ref. 13
Ref. 71
Ref. 25
Ref. 16
Ref. 12
Ref. 24
Ref. 48
Ref. 23
Ref. 13
Ref. 10
Ref. 55
Ref. 18
Ref. 11
Ref. 14
Ref. 24
Ref. 23
Ref. 22
J_{sc} (mA cm^{-2})
V_{oc}*FF (V)
b
ETL
Top interface
Top surface
Bulk
Bottom surface
Buried interface
HTL
c
HTL
Perovskite
ETL
QFLS
d
Sn^{2+} - 2e$^-$ → Sn^{4+}
V_{Sn}
Sn oxidation
e
Air exposure
Sn^{2+} → Sn^{4+}
Without Sn
Air exposure
Sn^{4+}+Sn → 2Sn^{2+}
With Sn
f
Bulk Crystallization
g
Antisolvent
Gas quench
1 μm
h
Interface recommbination
i
HAADF
Pb
Sn
Full-lead WBG
Pb-Sn NBG
50 nm
j
V_A
V_X
Surface passivation
k
Control
PDA treated
500 nm
Potential (mV)
30
−30
l
Buried anchoring
m
PEDOT:PSS
2F
Potential (mV)
300
150
500 nm
Perovskite
ETL
Substrate
Heterostructure
HTL
Grain boundry engineering
Surface passvation
PEA$^+$
EDA^{2+}
A site
B site
X site
Perovskite structure
Hole
Electron

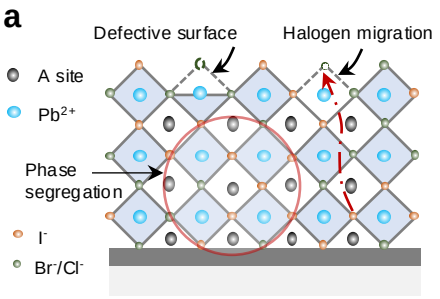
a
Defective surface
Halogen migration
A site
Pb2+
Phase segregation
I-
Br-/Cl-

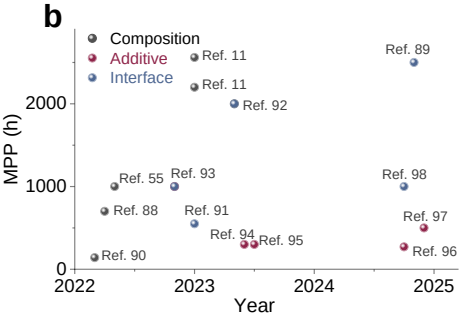
b
Composition
Additive
Interface
MPP (h)
Year
Ref. 89
Ref. 11
Ref. 11
Ref. 92
Ref. 55
Ref. 93
Ref. 98
Ref. 88
Ref. 91
Ref. 97
Ref. 94
Ref. 95
Ref. 90
Ref. 96

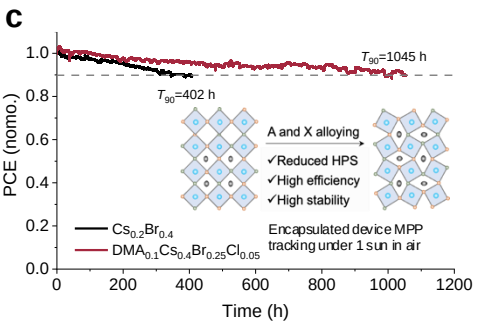
c
T90=1045 h
T90=402 h
PCE (nomo.)
Time (h)
A and X alloying
✓Reduced HPS
✓High efficiency
✓High stability
Cs0.2Br0.4
DMA0.1Cs0.4Br0.25Cl0.05
Encapsulated device MPP tracking under 1 sun in air

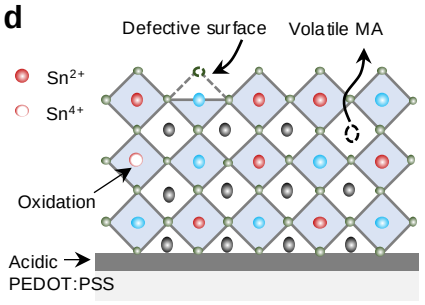
d
Defective surface
Volatile MA
Sn2+
Sn4+
Oxidation
Acidic
PEDOT:PSS

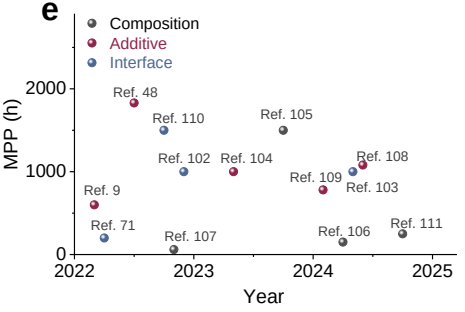
e
Composition
Additive
Interface
MPP (h)
Year
Ref. 48
Ref. 110
Ref. 105
Ref. 102
Ref. 104
Ref. 108
Ref. 109
Ref. 103
Ref. 9
Ref. 71
Ref. 107
Ref. 106
Ref. 111

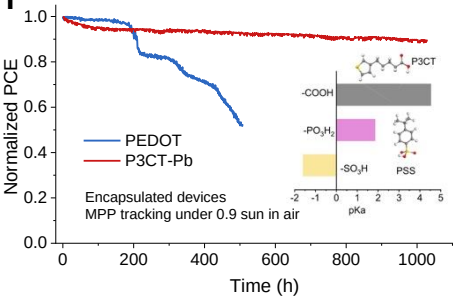
f
Normalized PCE
Time (h)
PEDOT
P3CT-Pb
Encapsulated devices
MPP tracking under 0.9 sun in air
P3CT
-COOH
-PO3H2
-SO3H
PSS
pKa

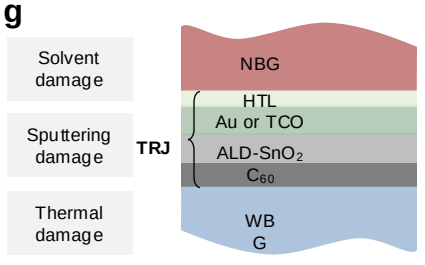
g
Solvent damage
Sputtering damage
Thermal damage
TRJ
NBG
HTL
Au or TCO
ALD-SnO2
C60
WB
G

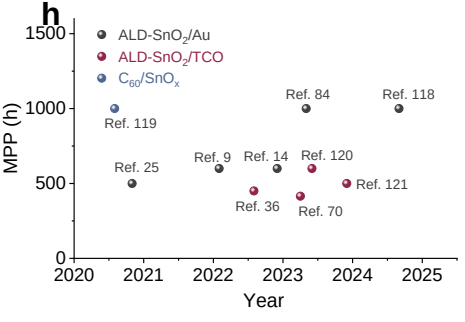
h
ALD-SnO2/Au
ALD-SnO2/TCO
C60/SnOx
MPP (h)
Year
Ref. 84
Ref. 118
Ref. 119
Ref. 25
Ref. 9
Ref. 14
Ref. 120
Ref. 121
Ref. 36
Ref. 70

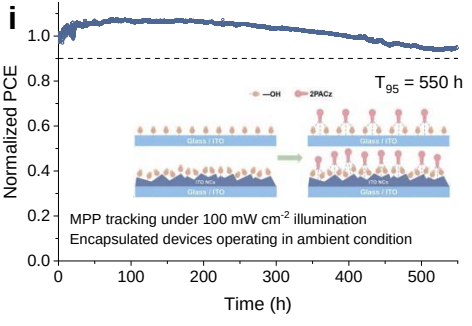
i
T95 = 550 h
Normalized PCE
Time (h)
MPP tracking under 100 mW cm-2 illumination
Encapsulated devices operating in ambient condition

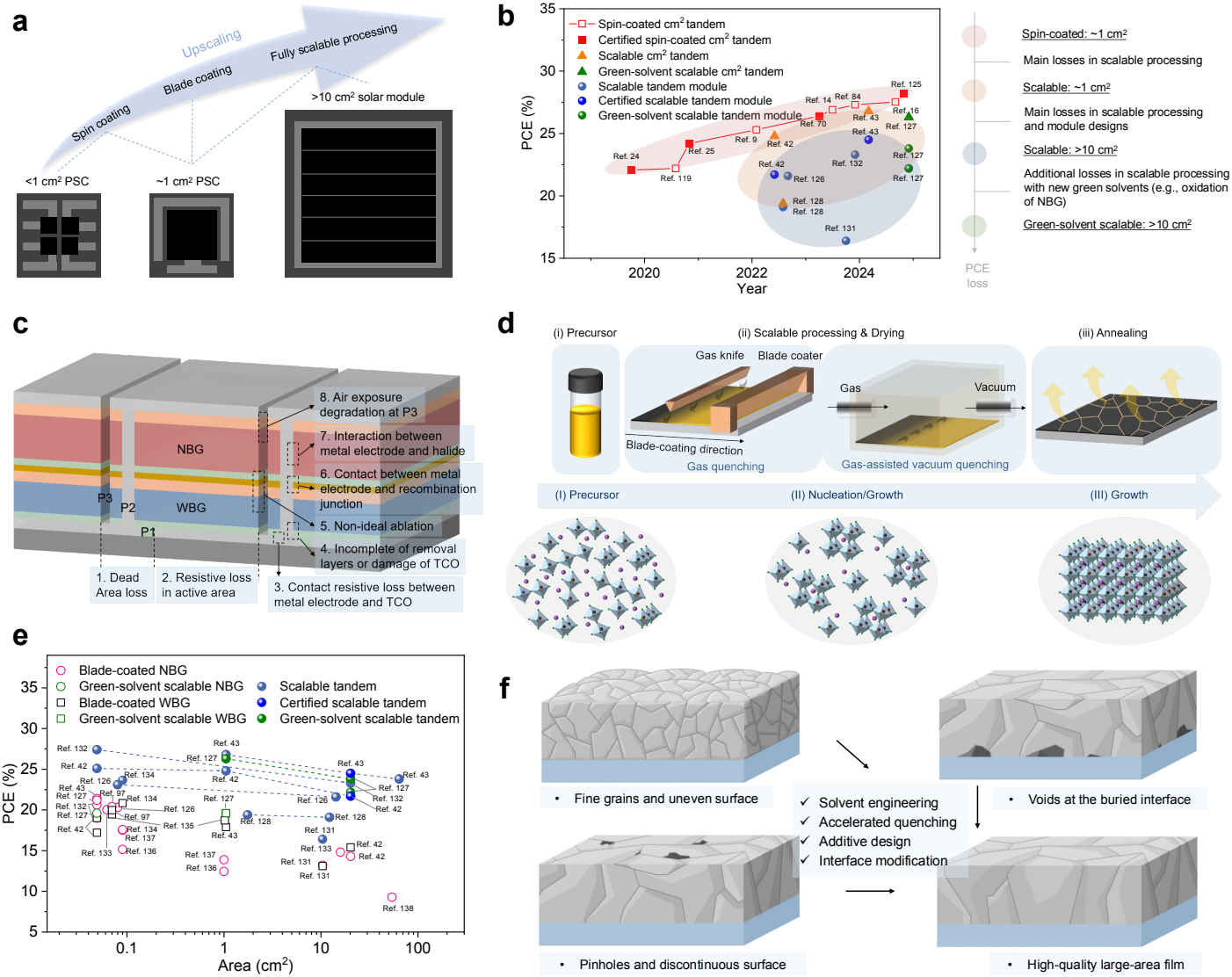
a
Upscaling
Fully scalable processing
Blade coating
Spin coating
>10 cm² solar module
<1 cm² PSC
~1 cm² PSC
b
Spin-coated cm² tandem
Certified spin-coated cm² tandem
Scalable cm² tandem
Green-solvent scalable cm² tandem
Scalable tandem module
Certified scalable tandem module
Green-solvent scalable tandem module
PCE (%)
Year
Spin-coated: ~1 cm²
Main losses in scalable processing
Scalable: ~1 cm²
Main losses in scalable processing and module designs
Scalable: >10 cm²
Additional losses in scalable processing with new green solvents (e.g., oxidation of NBG)
Green-solvent scalable: >10 cm²
PCE loss
c
NBG
WBG
P1
P2
P3
8. Air exposure degradation at P3
7. Interaction between metal electrode and halide
6. Contact between metal electrode and recombination junction
5. Non-ideal ablation
4. Incomplete removal layers or damage of TCO
1. Dead Area loss
2. Resistive loss in active area
3. Contact resistive loss between metal electrode and TCO
d
(i) Precursor
(ii) Scalable processing & Drying
(iii) Annealing
Gas knife
Blade coater
Blade-coating direction
Gas quenching
Gas
Vacuum
Gas-assisted vacuum quenching
(I) Precursor
(II) Nucleation/Growth
(III) Growth
e
Blade-coated NBG
Green-solvent scalable NBG
Blade-coated WBG
Green-solvent scalable WBG
Scalable tandem
Certified scalable tandem
Green-solvent scalable tandem
PCE (%)
Area (cm²)
f
Fine grains and uneven surface
Voids at the buried interface
Solvent engineering
Accelerated quenching
Additive design
Interface modification
Pinholes and discontinuous surface
High-quality large-area film

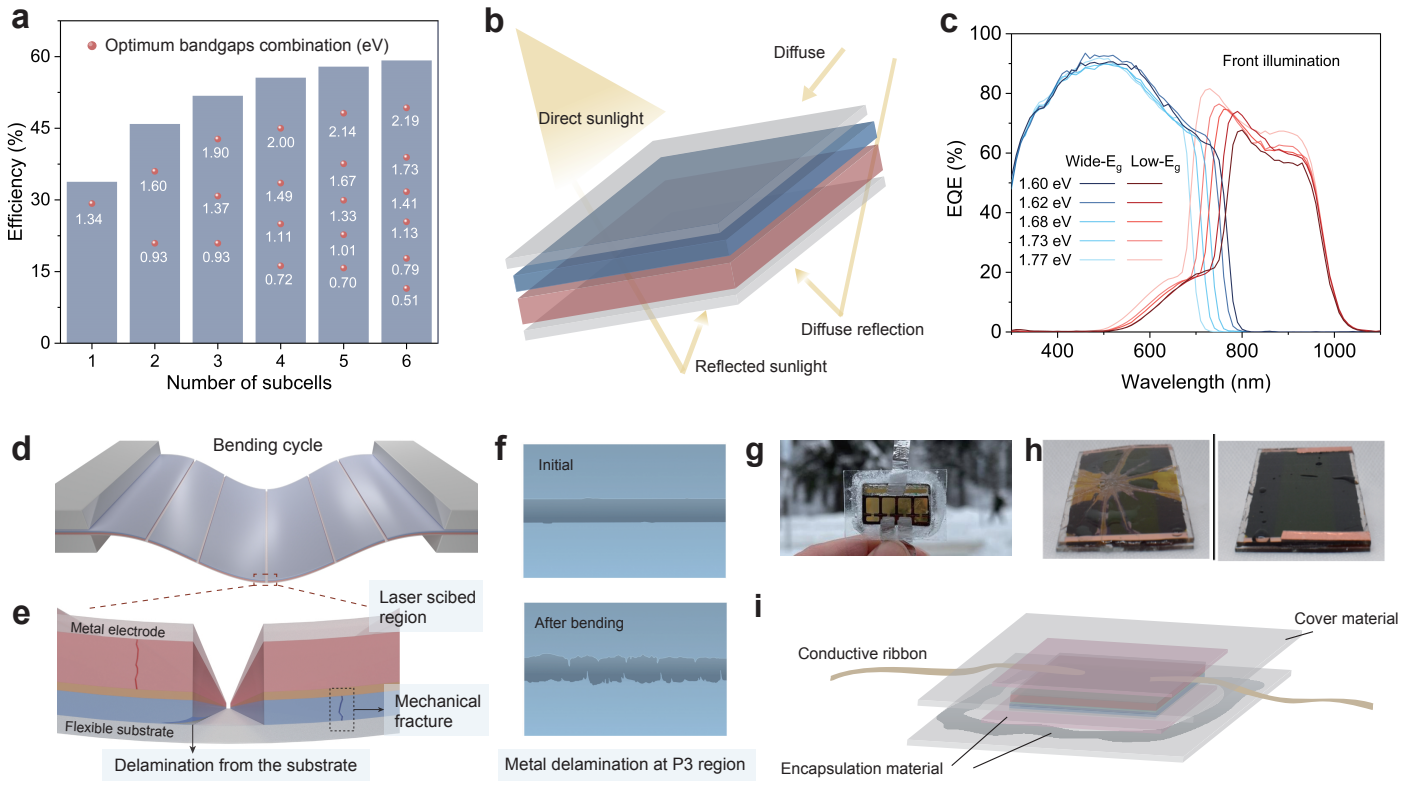
a
Optimum bandgaps combination (eV)
Efficiency (%)
Number of subcells
1.34
1.60
0.93
1.90
1.37
0.93
2.00
1.49
1.11
0.72
2.14
1.67
1.33
1.01
0.70
2.19
1.73
1.41
1.13
0.79
0.51
b
Diffuse
Direct sunlight
Diffuse reflection
Reflected sunlight
c
Front illumination
EQE (%)
Wavelength (nm)
Wide-Eg Low-Eg
1.60 eV
1.62 eV
1.68 eV
1.73 eV
1.77 eV
d
Bending cycle
e
Laser scibed region
Metal electrode
Flexible substrate
Mechanical fracture
Delamination from the substrate
f
Initial
After bending
Metal delamination at P3 region
g
h
i
Cover material
Conductive ribbon
Encapsulation material